Highlighting the effect of heterogeneous blood perfusion on radio-frequency ablation of human brain tumors: An image-based numerical investigation

Ajay Bhandari[1, *], Siddhartha Mukharjee[1], Anand Kumar[1], Anup Singh[2,3] and Wenbo Zhan[4, *]

[1] Department of Mechanical Engineering, Indian Institute of Technology (Indian School of Mines) Dhanbad-826004, India

[2] Centre for Biomedical Engineering, Indian Institute of Technology Delhi, New Delhi 110016, India

[3] Department of Biomedical Engineering, All India Institute of Medical Sciences, New Delhi 110029, India

[4] School of Engineering, University of Aberdeen, Old Aberdeen Campus, Aberdeen AB24 3UE, UK

*Correspondence: ajayb@iitism.ac.in (AB); w.zhan@abdn.ac.uk (WZ)

Abstract:

Radio-frequency ablation (RFA) is a minimally invasive treatment that can provide highly localized and precise cancer therapy. Despite these advantages, its application in clinical practice remains limited. This is primarily due to the insufficient ablation volume, where blood perfusion plays a significant role. In this study, computational modeling is applied to examine the effects of heterogeneous blood perfusion on the tissue temperature, resultant thermal damage, and ablation volume in the RFA treatment. Two patients' heterogeneous blood perfusion and 3D brain tumor geometry are extracted from their dynamic contrast enhanced-magnetic resonance imaging (DCE-MRI) data. This patient-specific information is imported into the bioheat transfer model developed in OpenFOAM to predict thermal effects. Results show that the heterogeneous blood perfusion leads to deeper heat penetration in the tumor tissue compared to the simulation in which blood perfusion is assumed to be uniform across the entire tumor. On average, the predicted tissue temperature and ablation volume are 10-11% and 30-38% higher for both patients, respectively, when the heterogeneous blood perfusion is adopted. In addition, the ablation volume is highly susceptible to the applied RF voltage and coolant temperature. These two factors can be optimized to maximize the treatment. However, the optimal settings vary for each patient, highlighting the demand for patient-specific design. Results obtained from this study can assist clinicians and surgeons in optimizing RFA parameters for a specific patient that can improve the treatment efficacy.

Keywords: RFA, heterogeneous blood perfusion, DCE-MRI, ablation volume, human tumors

NOMENCLATURE

$\sigma(T)$	Temperature-dependent electrical conductivity
V	Electrical Potential
ρc	Heat capacity of the tissue
$\rho_{bl} c_{bl}$	Heat capacity of the blood
$k(T)$	Temperature-dependent thermal conductivity
$\omega_{bl}(r, \Theta)$	Blood perfusion rate as a function of space and thermal damage
r	Position vector describing a point in 3D space

Θ Thermal damage parameter.

T_{bl} Blood temperature.

T Tissue temperature.

q_m Metabolic heat generation rates due to external heating inside the tissue.

q_g Volumetric heat generation rates due to external heating inside the tissue.

A Frequency factor

ΔE Activation energy responsible for irreversible thermal coagulation.

R Universal gas constant.

$P(\Theta)$ Probability of observing thermal damage.

$(\rho c)_{vap}$ Heat capacity of water vapor.

ρ_w Water density

h_{fg} Latent heat of vaporization of water

β Tissue water content

T_l and T_u Lower and upper phase change temperatures, respectively.

σ_o and k_0 Initial electrical and thermal conductivities inside the tumor and normal tissues, respectively.

T_{body} Initial body temperature

T_{avg} Spatial-averaged temperature

$Z(t)$ Tissue impedance

$I(0)$ Signal intensity (SI) without contrast agent (CA)

$I(t)$ SI at a particular time point after administration of CA

TR Repetition time

TE Echo time

θ Flip angle

T_1 Spin-Lattice relaxation time

T_2 Spin-spin relaxation time

R_1 Longitudinal relaxivity of CA

R_2 Transverse relaxivity of CA

T_{10} Relaxation time without CA administration

$C_{Gd,ECS}(t)$	CA concentration in the interstitial space.
R(t)	Time-dependent residue curve
$C_a(t)$	CA concentration inside the blood plasma
h_{cool}	Convective heat transfer coefficient
T_{cool}	Coolant temperature at the surface of the active electrode tip.
$\vec{n}$	Unit normal vector
V_T	Total tumor tissue volume.

Abbreviations

RFA	Radiofrequency ablation
FEM	Finite element method
DCE-MRI	Dynamic contrast-enhanced magnetic resonance imaging
FFE	Fast field echo
FSE	Fast spin echo
CA	Contrast agent
SI	Signal intensity
PD	Proton density
FLAIR	Fluid attenuated inversion recovery
SPGR	Spoiled gradient recalled echo
CBF	Cerebral blood flow
CFD	Computational fluid dynamics
PPMCC	Pearson product-moment correlation coefficient
PID	Proportionate-integral-derivative
TID	Thermal isoeffective dose
CEM	Cumulative equivalent minutes

1. Introduction:

RFA is a localized treatment method that uses radio frequency waves generated by a conductive probe to heat tissue. It has been widely applied in treating different cancers, including liver tumors [1] and brain tumors [2]. However, the shallow penetration depth of heat and insufficient tumor volume coverage significantly limits clinical use. These limitations can partially be attributed to the microvascular blood perfusion (localized blood flow through the capillaries), which substantially contributes to the convection of heat from the tissue by the

blood ("the heat sink effect"). The distribution and rate of blood perfusion significantly affect the dimensions and shape of the ablation zone, thereby determining the therapeutic efficacy. Moreover, the role of blood perfusion becomes more dominant when the tissues are highly vascularized [3]. Therefore, it is imperative to understand the complex interplay among blood perfusion, tissue temperature, and thermal damage. Numerical modeling is an excellent tool to achieve this non-invasively.

Several studies on the numerical simulation of RFA in tumors have been reported in the literature, focusing on the impact of various influencing factors on the therapeutic efficacy of RFA treatment. These include the RFA control parameters [4], probe placement [5,6], number of probes [7], pulsing protocol [8], type of voltage [9,10], tissues [11], monitoring schemes [12], and probe switching [13,14]. Specifically, Haemmerich *et al.* developed a FEM-based computational model to simulate a temperature-controlled RFA using a PI controller and optimized the control parameters. This model using the optimized parameters, enabled effective control of RF ablation with minimal user input, facilitating the application of RFA [4]. Altrogge *et al.* optimized the placement of mono and bipolar RFA probes by minimizing a temperature-based objective function. The model prediction agreed well with the placement of the probe selected by the physician [5]. Moreover, a novel optimization strategy combined with FEM was proposed by Chen *et al.* to identify the optimal RFA probe placement. The robustness of the model was assessed in multiple scenarios involving single and multiple ablations. The algorithm was found with the potential to provide meaningful predictions that can assist clinicians in developing patient-specific treatment plans [6]. Furthermore, simulations have been carried out to combine a multi-probe RFA system with a surgical navigation system to establish a virtual surgical platform for RFA preoperative planning [7]. Trujillo *et al.* compared voltage and current pulses protocol to evaluate their ability to generate larger coagulation zone in impedance-controlled RFA procedures [8]. In addition to focusing on size, studies were performed to manipulate the shape of the coagulation zone in RFA treatments by adjusting the location of saline infusion. Results would improve the accuracy of targeting the tissue of interest [9]. Constant DC voltage was compared to low-frequency AC voltage in terms of the thermal impact efficacy to develop the voltage pulse protocol. AC voltage can result in thermal oscillations near the RF probe, however, the choice of voltage has limited effect on lesion depth [10]. A wide spectrum study using tumors located in lung, liver, kidney and breast demonstrated that RFA input parameters and therapeutic efficacy are highly sensitive to the tissue type, highlighting the need to develop tissue-specific RFA protocols [11]. Recently, effort has been made to simulate bipolar RFA techniques [13], impedance and time-based switching [14], and directional ablation [15] to enlarge the ablation volume. More importantly, novel artificial intelligence methods such as deep neural networks [16] reinforced with new loss functions [17] have also been explored to unveil the physics of conduction heat transfer, which is a fundamental part of RFA modeling studies.

Blood perfusion is one of the essential parameters that can significantly affect the therapeutic efficacy of RFA treatment. Many studies have been focused on investigating the variation in perfusion rates [18] in combination with other RFA parameters, such as electrical and thermal conductivity [19], and perfusion algorithms [20] to elucidate their effect on ablation volume. It

has been observed that the size of the coagulation zone strongly depends on the tumor's perfusion and surrounding normal tissue [18]. At the same time, the effect of blood perfusion on therapeutic efficacy can be minimized by optimizing the thermal and electrical conductivity combinations for every patient [19]. Previous studies assumed the blood perfusion either to be constant or a function of ablation time and temperature, with its spatial dependency, neglected. However, blood perfusion inside the tumor can be highly heterogeneous owing to the complex and chaotic tumor microvasculature [21,22]. The blood perfusion rate and distribution of microvasculature vary considerably among patients [23], raising the demand for tailoring the pre-treatment RFA protocol for each patient. Disappointingly, this question remains unsolved. In this regard, it is crucial to investigate how the heterogeneous blood flow inside the tumor capillaries affects the tissue temperature and thermal damage in RF treatment.

Motivated by this, the current study employs an image-based computational model to predict the therapeutic efficacy of the RFA procedure in human brain tumors using heterogeneous blood perfusion. The spatially dependent heterogeneous perfusion and 3D tumor geometry are extracted from DCE-MRI data and are used as input into the computational model. A comparison of the therapeutic efficacy between the simulations using heterogeneous and homogeneous blood perfusion has been conducted in terms of thermal damage, heat penetration, and ablation ratio. The impact of RF voltage, coolant temperature, and their cross-impact on thermal damage has also been demonstrated. Furthermore, the DCE-MRI data of two patients have been analyzed to investigate the impact of inter-patient blood perfusion variation on RFA treatment efficacy and control parameters.

2. Methods and Materials

2.1 Mathematical model

Simulating RFA is a coupled mathematical problem involving developing models for the electric field, temperature distribution, and their interplay. Since RFA frequency is located in the range of 450-550 kHz [24]. The wavelength of the electric field is an order of magnitude higher than the active electrode size. Moreover, the electric field's timescale is much smaller than the thermal field's. Therefore, the electric potential distribution can be approximated using the quasi-static assumption, expressed as [25]

$$\nabla \cdot (\sigma(T)\nabla \mathrm{V}) = 0 \tag{1}$$

The heat transfer in the tissue has been modeled using Pennes' bioheat equation, which can accurately capture the temperature distribution in the tissues in the most simplified manner [26]

$$\rho c \frac{\partial \mathrm{T}}{\partial t} = \nabla \cdot (k(T)\nabla \mathrm{T}) - \rho_{bl} c_{bl} \omega_{bl}(r,\Theta)(T - T_{bl}) + q_m + q_g \tag{2}$$

The metabolic heat generation rate has been neglected in the current study due to its small magnitude as compared to the volumetric heat generation rate, which is expressed as [25]

$$q_g = \sigma(T)|\nabla V|^2 \tag{3}$$

Tissue thermal damage has been predicted based on the thermal coagulation model, which is described by the Arrhenius first-order reaction kinetics [27] as

$$\frac{d\Theta(r,t)}{dt} = Ae^{\frac{-\Delta E}{RT(r,t)}} \quad (4)$$

$P(\Theta)$ can be computed as follows [28]

$$P(\Theta) = 100\%(1 - e^{-\Theta}) \quad (5)$$

where $P(\Theta)$ tends to 100% when $\Theta \geq 4.6$.

2.1.1 Model parameters

The RFA of a brain tumor is simulated in the current study. Summarized in Table 1 are the parameters for a brain tumor and normal brain tissue used in equations (1)-(5). All the parameters are assumed to be constant and thermally isotropic except for heat capacity, electrical and thermal conductivity, and blood perfusion.

Table 1: Model parameter values for tumor and normal tissue

Symbol	Unit	Brain tumor	Normal tissue
ρ	kg/m^3	1031.45 [29]	1031.45 [29]
c	J/kg·K	3640 [29]	3640 [29]
k	W/m·K	0.534 [29]	0.534 [29]
σ	S/m	0.2 [30]	0.0751 [30]
ω_{bl}	ml of blood/sec· ml of tissue	Calculated from DCE-MRI	
ρ_{bl}	kg/m^3	994 [13]	994 [13]
c_{bl}	J/kg·K	4180 [13]	4180 [13]
$(\rho c)_{vap}$	J/ m^3·K	6×10^5 [9]	6×10^5 [9]
A	1/s	3.247 E43 [13]	7.39E 39 [13]
ΔE	kJ/mol	281.4 [13]	257.7 [13]
β	-	0.77 [13]	0.77 [13]
h_{fg}	MJ/kg	2.258 [13]	2.258 [13]
T_l	ºC	99 [13]	99 [13]
T_u	ºC	100 [13]	100 [13]
T_{body}	ºC	37	37
R	J/mol·K	8.314 [13]	8.314 [13]

In RFA, it is possible that tissue temperature goes beyond 100ºC, leading to water vaporization inside the tissue. To account for these thermal effects, the heat capacity of the tissue has been updated as follows [25]

$$\rho c = \begin{cases} \rho c & T \leq T_l \\ \frac{1}{2}[\rho c + (\rho c)_{vap}] + \frac{\rho_w h_{fg} \beta}{T_u - T_l} & T_l < T \leq T_u \\ (\rho c)_{vap} & T > T_u \end{cases} \quad (6)$$

For temperature dependence of electrical conductivity, a rapid drop in conductivity of a factor of 10,000 has been assumed when the temperature reaches or exceeds 100ºC. Electrical conductivity increases with a temperature coefficient of 2% per 1ºC [31]. The thermal conductivity is supposed to increase at a rate of 0.00165W/mK per 1ºC increase in temperature [13]. The following equations have been employed to model the temperature dependence of electrical and thermal conductivity.

$$\sigma(T) = \begin{cases} \sigma_0[1 + 0.02(T - T_{body})] & T \leq T_u \\ 0.0001\ \sigma_0 & T \geq T_u \end{cases} \quad (7)$$

$$k(T) = \begin{cases} k_0 + 0.00165(T - T_{body}) & T \leq T_u \\ k_0 + 0.00165(T_u - T_{body}) & T > T_u \end{cases} \quad (8)$$

Coagulation starts as the tissue temperature increases in RFA, leading to changes in blood perfusion. It has been reported that when the heating commences, the blood perfusion initially increases due to vasodilation of the capillaries and then decreases with heat-induced damage. To account for this phenomenon, the dependence of blood perfusion on thermal damage can be expressed as [32]

$$\omega_{bl}(r, \Theta) = \begin{cases} \omega_{bl}(r) & \Theta \leq 0 \\ \{\omega_{bl}(r)[1 + 2500(\mathrm{t}) - 2600^2(t)] & 0 < \Theta < 0.1 \\ \omega_{bl}(r)\exp(-\Theta(\mathrm{t})) & \Theta \geq 0.1 \end{cases} \quad (9)$$

Unlike normal tissues, blood flow in tumor tissues cannot be enhanced in response to temperature rise. In this regard, a more conventional expression for the blood perfusion in the tumor has been adopted [13]

$$\omega_{bl}(r, \Theta) = \begin{cases} \omega_{bl}(r) & \Theta < 4.6 \\ 0 & \Theta \geq 4.6 \end{cases} \quad (10)$$

The initial rate of heterogeneous blood perfusion $\omega_{bl}(r)$ has been extracted from the patient DCE-MRI data and mapped to each voxel of the 3D model geometry using the coordinates. The voxels of the tumor and normal tissue in the domain are identified based on the mapping. The rest model parameters, as described in Table 1, are then assigned accordingly. The MR images include voxels outside the brain, which belong neither to the tumor nor to the normal brain tissue. These voxels are exterior voxels corresponding to air, and all model parameter values are assigned zero.

An impedance-controlled pulsing protocol has been implemented to eradicate the effects of tissue charring due to RFA overheating. In this protocol, once the tissue impedance crosses a pre-set threshold, the RF power is switched off for a predetermined time, known as roll-off time. The tissue gets cooled during this time, and the deposited water vapor on the electrode surface gets diffused, facilitating the smooth flow of the RF current. The tissue impedance at each time is calculated by [33]

$$Z(t) = \iiint \frac{V^2}{q_g} dV \quad (11)$$

In the current study, it has been assumed the roll-off occurs when the tissue impedance increases by 30 Ω above the initial impedance [34]. The roll-off time has been taken to be 15 sec, consistent with previous studies [8].

2.2 MR imaging and processing protocol

MR data of two brain tumor patients were acquired using a 3.0-Tesla MRI scanner (Philips Healthcare, Amsterdam, The Netherlands) at Fortis Memorial Research Institute, Gurugram, India. DCE MRI data acquisition as a part of a retrospective study was performed through the 3D T1-FFE sequence before, during, and after the administration of Dotarem (Gadoterate meglumine, Guerbet, France). The dose was $0.1\ \mathrm{mmol/kg}$ body weight and the infusion rate was $3.0\ \mathrm{mL/s}$. In addition to perfusion MRI, routine MRI data, including standard sequences such as T1-weighted, T2-weighted, 3D FLAIR, and post-contrast T1-weighted, were also acquired. The key imaging parameters are summarised in Table 2. All procedures involving human participants performed in this study were approved by the Institutional ethics committee and followed the ethical standards of the Institutional Review Board (IRB No. 2020-001-19-28). Written informed consent was obtained from each subject before acquisition.

Table 2: T1-perfusion MR image acquisition protocol

Parameter	Unit	Value
TR	ms	6.27
TE	ms	3.0
θ	deg	10
Field of view	mm	230×230
Slice thickness	mm	6.0
Number of slices	NA	12
Reconstruction matrix	NA	256×256
Time of acquisition	min	2.15
Temporal resolution	sec	3.8

The demographic characteristics of the two exemplary patients are given in Table 3.

Table 3: Demographic details of the patient

Demographic characteristics	Patient 1	Patient 2
Gender	M	F
Age	67	72
Tumor type	Glioblastoma	Meningioma
Newly diagnosed or recurrent tumor	Newly diagnosed	Newly diagnosed
Tumor grade	IV	I

2.2.1 3D reconstruction of brain tumor and RF probe geometry

A representative T1-weighted pre- and post-contrast image MR slice and the reconstructed 3D geometry are shown in Figure 1. The brain tumor is segmented from its surrounding brain tissue based on the local SI of the image slice. The segmentation results are stacked along the MR scan direction to reconstruct the 3D geometry (Figure 1(d)). The contrast-enhancing volume of the brain tumor is measured as 57833.8 mm^3. Given that the focus of the study is to investigate the effect of blood perfusion heterogeneity on RFA treatment against the tumor rather than the surrounding tissue, a rectangular domain (Figure 1(c)) with the dimensions of $58 \times 97 \times 72$ mm^3 is constructed to enfold the brain tumor fully. The final computational mesh consists of 331,776 structured elements obtained after the grid-independence test, with details provided in Appendix A. The RFA probe (illustrated in white color in Figure 1(d)) is inserted through the center of the domain along the z-axis. The geometry of the probe is adapted from the recommendations of Ref. [4,35]. A square-shaped, internally cooled electrode is modeled. The conducting length is 12 mm covering two image slices. The side length is 1.8 mm, which is in line with Ref. [35].

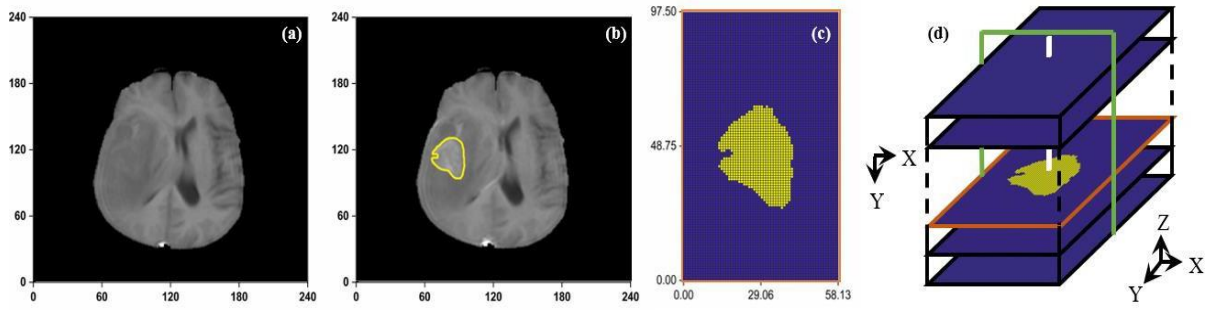

Figure 1. Model geometry. (a) pre-contrast and (b) post-contrast MR image of a representative slice with a yellow outline showing tumor boundary. (c) The segmentation result and mesh where the tumor and its holding tissue are marked in yellow and blue, respectively (All dimensions in mm). (d) Schematical diagram showing the 3D geometry reconstruction with RF probe marked white. Modeling results will be presented in the X-Z plane that is along the RF probe track in the following sections, marked in green color.

2.2.2 Extraction of heterogenous blood perfusion

DCE-MRI data quantification is performed by estimating the concentration of CA (Dotarem) from the SI of the T1-dynamic images on a voxel-by-voxel basis. The pre-contrast T1 (T_{10}) value is also estimated to aid the quantification. This is based on the SPGR/FFE equation [23] that is represented as

$$\frac{I(t)}{I(0)} = k_0 \exp[-TER_2 C_{\mathrm{Gd,ECS}}(t)] \frac{1-\exp\{-TR[T^{-1} + R_1 C_{\mathrm{Gd,ECS}}(t)]\}}{1-\cos(\theta)\exp\{-TR[T_{10}^{-1} + R_1 C_{\mathrm{Gd,ECS}}(t)]\}} \quad (12)$$

$$k_0 = \frac{1-\cos(\theta)\exp(-TRT_{10}^{-1})}{1-\exp(-TRT_{10}^{-1})} \quad (13)$$

The R_1 and R_2 of Dotarem in the plasma are 3.5 $mmol^{-1}s^{-1}L$ and 4.9 $mmol^{-1}s^{-1}L$, respectively. T_{10} is estimated using the three FSE images, including T1-weighted images ($TR = 360\ ms,\ TE = 10\ ms$), T2-weighted images ($TR = 3500\ ms,\ TE = 90\ ms$) and PD-weighted images ($TR = 3500\ ms,\ TE = 7.2\ ms$). Readers can refer to Ref. [23] for details. The rest imaging parameters for acquiring T1-weighted, T2-weighted, and PD-weighted images are the same as for T1-perfusion MR images, as summarized in Table 2. Once the concentration-time curves for each voxel ($C_{\mathrm{Gd,ECS}}(t)$) are estimated, the hemodynamic parameter named CBF or the blood perfusion can be estimated at each voxel by

$$C_{\mathrm{Gd,ECS}}(t) = \rho \cdot H \cdot CBF \cdot (C_{\mathrm{a}}(t) \otimes R(t)) \tag{14}$$

where $\otimes$ represents the convolution operation. *R(t)* and $C_a(t)$ have been estimated using the procedure mentioned in Ref. [36]. H accounts for the difference in hematocrit between capillaries (H_{cap} = 25%) and large arteries (H_{art} = 25%) and is defined as

$$H = \frac{(1-H_{art})}{(1-H_{cap})} \tag{15}$$

Equation (14) needs to be deconvoluted to isolate CBF·R(*t*) for estimating CBF. Readers are recommended to refer to Ref. [23] for the details of the deconvolution method. The pre-contrast and post-contrast images and the blood perfusion contours are represented in Figure 2.

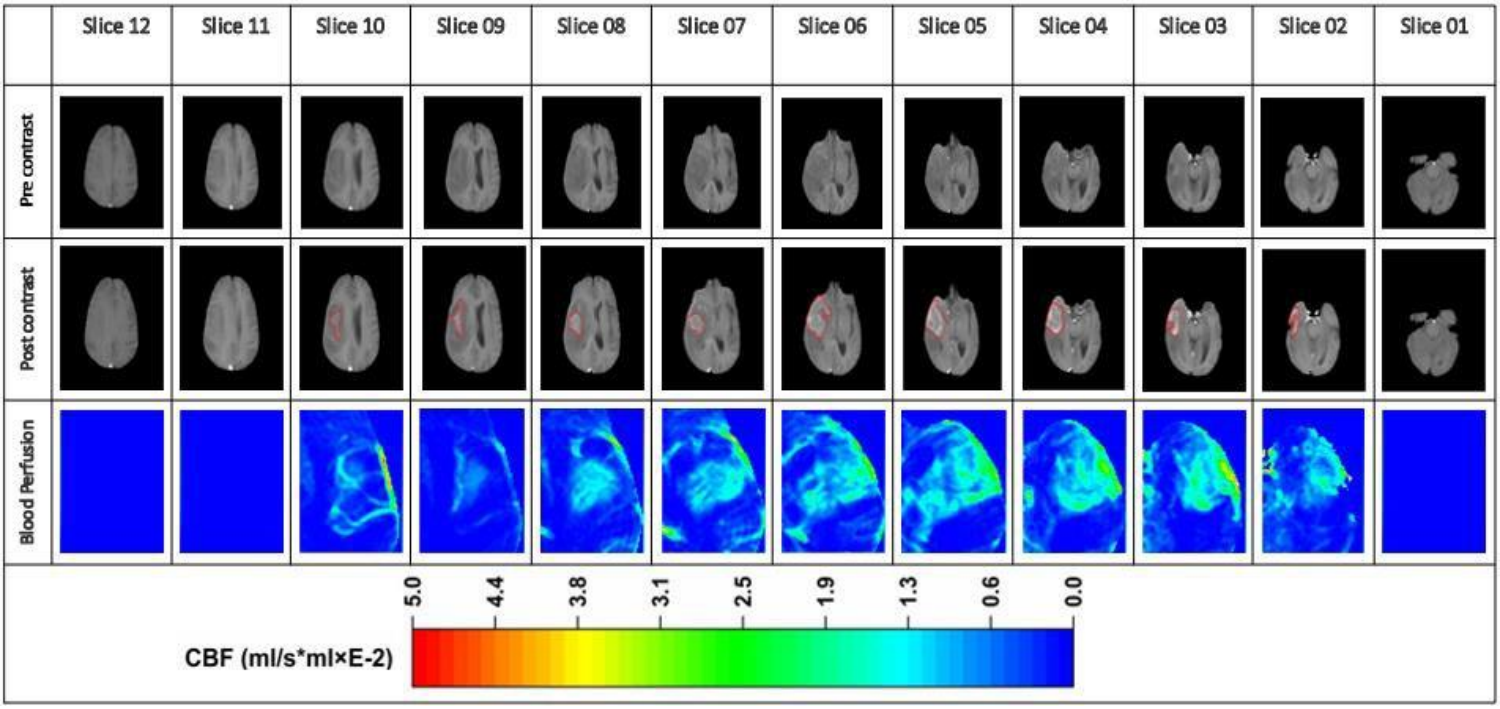

Figure 2. Tissue heterogeneous properties extracted from patient DCE-MR images. The interface between the brain tumor and its holding tissue is marked in red in the post-contrast images.

2.3 Numerical methods

The governing equations are solved using OpenFOAM, an open-source CFD code package based on finite volume methodology. The Laplace equation of potential is solved first to calculate the external heat generated by the RF probe that goes as input in Pennes' bioheat equation. The first-order Euler scheme is used to discretize the transient term as it is an implicit and unconditional scheme with no restriction on the time step. The Gauss linear and linear interpolation schemes are employed to discretize the gradient, and Laplacian terms, respectively. Geometric-algebraic multi-grid solver is used to solve electric potential equations, and the smooth solver with Gauss-Seidel smoother is used to solve the temperature equation. The tolerance limits are set as 1.0×10^{-8} for both the electric potential and temperature distribution models. No non-orthogonal correction is applied because an orthogonal grid is used in the study. The blood perfusion values extracted from DCE-MRI for heterogeneous modeling are mapped onto the CFD grid voxel-wise since both the image and grid are in cartesian coordinates, ensuring no potential offset. All the model parameters mentioned in Table 1 are separately set at each voxel (as per tumor and normal) by declaring these as non-uniform fields in OpenFOAM. After the time step-independence test, a fixed time step of 1 sec is selected, and simulations are carried out for 720 sec of physical time (standard ablation time) [37]. After each time step, the tissue impedance is calculated to check whether it exceeds the threshold value to initiate roll-off. During the roll-off period, the simulation keeps running with the external heat generation term (q_g) being switched off. All the numerical simulations are performed using AMD Ryzen 9 5900X processor with a clock speed of 3.70 GHz, twelve cores, with 32 GB RAM. The total computational time involved in solving the governing equations is approximately 2 hours.

2.3.1 Boundary and initial conditions

A zero-volt electric potential is applied at the external boundaries of the normal tissue that biologically signifies the ground pad in RFA. A Dirichlet boundary condition of fixed voltage (40V for baseline study) is imposed on the active boundaries of the RFA probe. For the temperature, the external boundaries of the normal tissue are assumed to be at normal body temperature (37ºC). Across the active boundaries of the RFA probe, a convective boundary condition is employed to replicate the internally cooled condition that can be expressed as

$$-k\frac{\partial T}{\partial \vec{n}} = h_{cool}(T - T_{cool}) \tag{16}$$

In the current study, h_{cool} and T_{cool} are set as 2496 W/m^{2}K and 10ºC, respectively, assuming the coolant flow rate through the electrode to be 45 ml/min [13]. The inactive boundary of the RF probe is considered to be electrically and thermally insulated. Initially, the electric potential and the temperature across the entire tissue domain are 0V and 37 ºC, respectively.

2.4 Quantification of RFA treatment

The following quantification indexes from the perspectives of heat penetration, heat distribution, and therapeutic efficacy are used to assess the effectiveness of the RFA treatment.

2.4.1 Spatial-averaged temperature

The tissue temperature directly reflects the amount of heat penetrated inside the tissue. It is simulated by Pennes' bioheat equation and varies throughout the brain tumor and its surrounding tissue, subject to heterogeneous blood perfusion. T_{avg} is applied to evaluate the heat penetration in the entire tissue, which is expressed as

$$T_{\text{avg}} = \frac{\sum T_{\text{i}} V_{\text{i}}}{\sum V_{\text{i}}} = \frac{\sum T_{\text{i}} V_{\text{i}}}{V_{\text{T}}} \tag{17}$$

where T_{i} and V_{i} are the local temperature and the local tissue volume, respectively. Index 'i' represents each control volume of the tumor region in the computational grid.

2.4.2 Location of distance course

As mentioned above, the tumor microenvironment is highly heterogeneous and varies considerably from the RFA probe site to the tumor periphery, presenting a non-uniform distribution. To quantify this spatial change, the location of the distance course (ψ_{dis}) is applied, which is expressed as

$$\psi_{\text{dis}} = \frac{\sum \psi_{\text{i}} V_{\text{i}}}{\sum V_{\text{i}}} \tag{18}$$

where ψ is the variable of interest and dis is the distance between the RFA probe site and local tissue volume.

2.4.3 Thermal damage volume (Ablation volume)

The thermal damage volume (ablation volume) reflects RFA therapeutic efficacy. It is calculated by taking the volume integral of all the voxels inside the tumor tissue domain with values of $\Theta \geq 4.6$.

2.4.4 Ablation Ratio (AR)

The ablation ratio is defined as the ratio of the ablation volume to the total tumor volume. It is defined as

$$AR = \frac{Ablation\ volume}{Total\ tumor\ volume} \tag{19}$$

2.5 Model validation

The present model is compared to the experimental results reported in Ref. [34] and [38] to validate its predictive power. In Ref. [34], RFA *ex vivo* experiments were conducted on fresh bovine liver tissue using an internally cooled electrode, and electrode temperature at different locations was measured using thermocouples. Along with the temperature, tissue impedance was also calculated to investigate the effect of roll-off. The model presented in Section 2.1 was applied while removing the blood perfusion term from Pennes' bioheat equation. The electrode dimensions, RF voltage, coolant flow rate, and coolant temperature were kept the same as in Ref. [34]. The model parameters listed in Table 1 were used for the liver tissue. The time course of modeling predicted tissue impedance is presented in Figure 3 against the experimental measurement. The PPMCC is calculated as 0.9, indicating a good agreement between the modeling and experiment. Furthermore, the predictions of the time for tissue impedance to plateau, start increasing and reaching its initial value again almost coincide with those reported in Ref. [34]. Some minor discrepancies between the predicted and experimental results may be due to different tissue geometry and probe placement mismatch between simulation and experiment. Another validation study on the thermal damage volume was performed in line with the RFA experiments reported in Ref. [38]. The details of the experiment in Ref. [38] are similar to that in Ref. [34]. The predicted thermal damage was found to be 19.92 cm^3, which is well located in the experimental range of 18~22 cm^3. These comparisons demonstrate the ability of the developed model to simulate the thermal ablation of heterogeneous tumors.

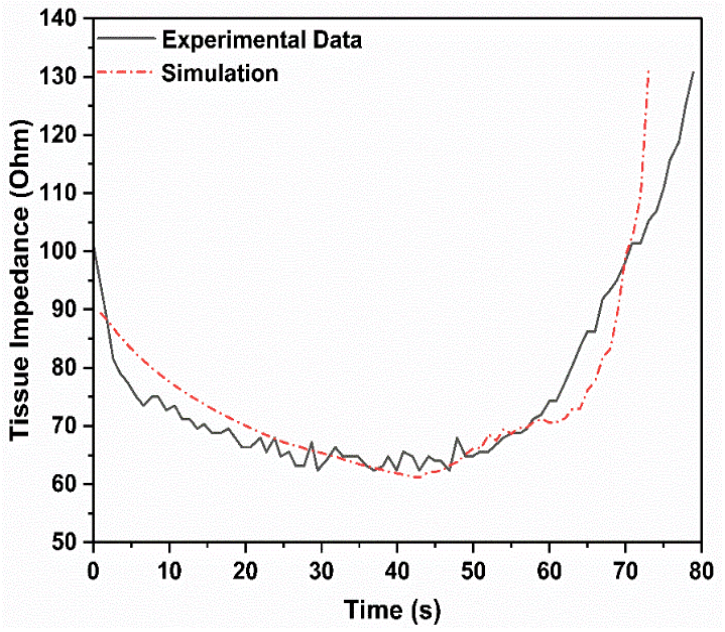

Figure 3. Comparison of experimentally measured and modeling predicted tissue impedance in RFA of liver tissue. Experimental data is extracted from Figure 6 in Ref. [34].

3. Results

3.1 Baseline study (Importance of blood perfusion heterogeneity)

The heat sink effect locally changes within the tumor due to perfusion heterogeneity, thereby altering the RFA therapeutic outcomes. A baseline study has been performed in which the RFA voltage and coolant temperature are 40V and 10ºC, respectively. Two simulations are conducted: (1) the heterogeneous case where the patient's realistic blood perfusion values extracted from DCE-MRI are mapped at each voxel in the computational domain; (2) the homogeneous case where uniform blood perfusion is assumed across the entire tumor, with the value set as the volume-averaged blood perfusion rate of the heterogeneous case. Simulated results using Patient 1 data are shown below. The results for Patient 2 are given in Appendix B.

The predicted temperature distribution and isotherms for the heterogeneous and homogeneous case at the end of the treatment (720 sec) are represented in Figures 4(a) and 4(b), respectively, on a vertical plane along the probe. In both cases, the tissue temperature decreases gradually from the heating probe towards the tumor periphery. It should be noted that the temperature at the probe-tissue interface is low. This is due to the cooling mechanism of the probe, which is applied to avoid the probe being overheated. A further comparison between these two simulations demonstrates that, in the heterogeneous case, heating can penetrate deep into the tumor tissue to cover a larger region for ablation. On the contrary, the heated region is underestimated in the homogeneous case. The predicted temperatures are further compared on a transverse line (marked in black color) drawn across the tumor tissue and heating probe, as shown in Figure 4(e). This closer look denotes that the value and the spread of tissue temperature are also underestimated if uniform blood perfusion is assumed in the entire tumor. Similar findings can be found for the thermal damage parameter (Θ) in Figures 4(c), (d), and (f), which reflect the treatment efficacy. Furthermore, the ablation ratio (AR) at the end of treatment was found to be 38% higher in the heterogeneous case than in the homogeneous case.

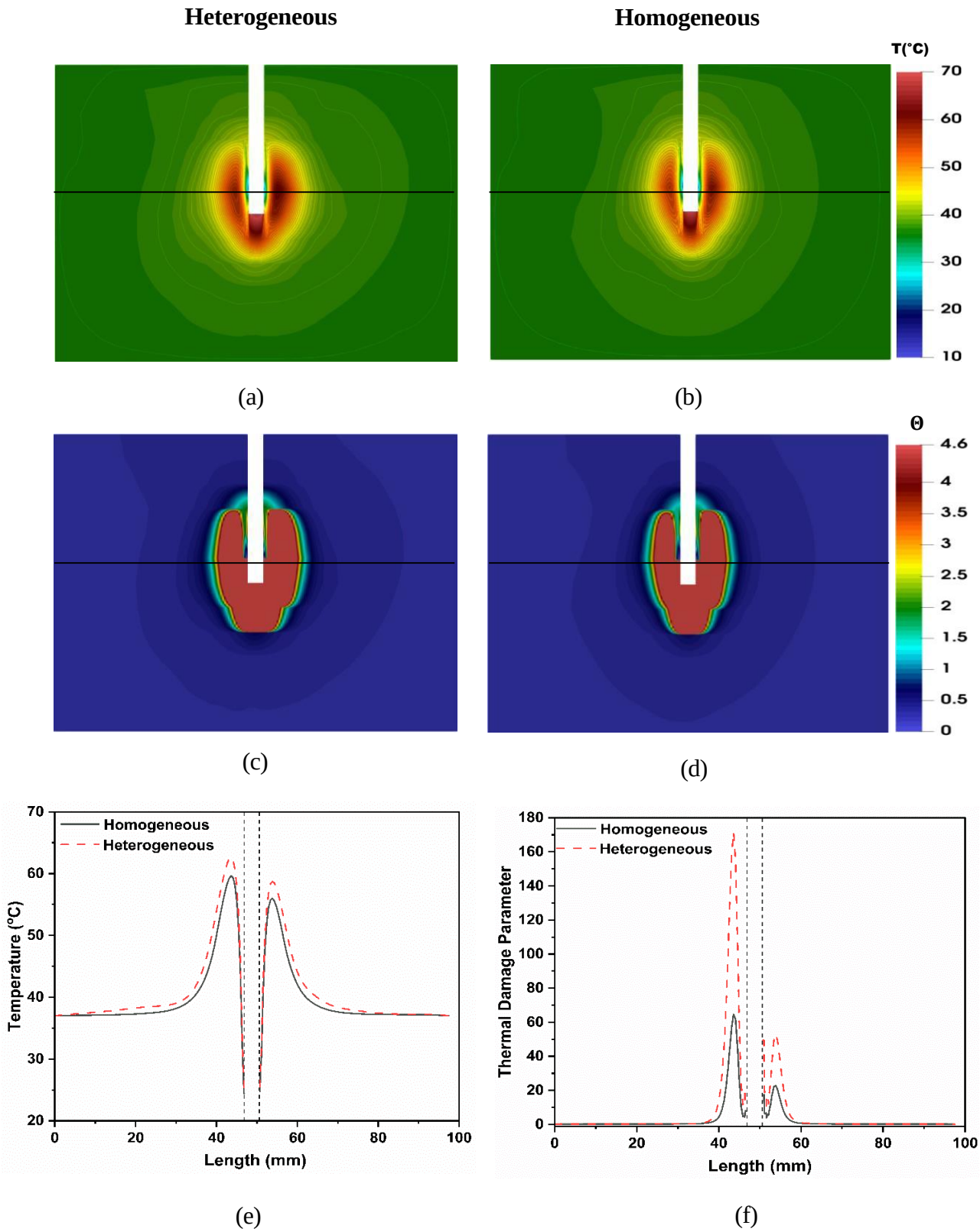

Figure 4. Contour plots of (a and b) Temperature and (c and d) thermal damage parameter for heterogeneous and homogeneous case. Line plots along the horizontal bisector of the slice (represented in white color) (e) Temperature and (f) Thermal damage parameter. Black dotted lines represent probe domain.

The heating outcomes are compared between the heterogeneous and homogeneous cases as a function of time in Figure 5. All variables are plotted using the volume-average values in the entire brain tumor, except for ablation volume which is defined in Section 2.4.3. Results show that both the tissue temperature (Figure 5 (a)) and ablation volume (Figure 5 (b)) are underestimated in the case where the assumption of uniform blood perfusion is used. The temperature difference in both cases is less pronounced in the first 60 sec because of insignificant changes in the tissue impedance (Figure 5 (c)) and external heating (Figure 5 (d)). Additionally, the ablation volume remains the same for up to 120 sec. This is because the tissue temperature is not high enough to trigger the thermal damage in the first 120 sec. However, as time proceeds, the ablation volume is underestimated in the homogeneous case, leading to the delay in the predicted starting time of thermal ablation. This is because of the higher heat sink effect ($W_g = \int \rho_{bl} c_{bl} \omega_{bl}(r, \Theta)(T - T_{bl}) \times dV$) as shown in Figure 5(f), where dV is the volume of each mesh element in the tumor region. The external heating source ($Q_g = \int q_g \times dV$) remains lower in the homogeneous case than in the heterogeneous one owing to the higher impedance. Since the tissue temperature and the volume of thermal ablation are determined by the trade-off between the external heating source and heat sink, the treatment outcome is underestimated in the homogeneous case. On average, the heat loss due to blood perfusion is 14% more in the homogeneous case than in the heterogeneous, resulting in approximately 30% less predicted ablation volume for the former at the end of the treatment.

Moreover, results show that blood perfusion remains constant in both cases for up to 120 sec (Figure 5 (e)), during which the thermal damage has not started. Once the thermal damage starts, the blood perfusion decreases over time due to coagulation. Comparisons show that the extent of the decrease is more significant in the heterogeneous case. A similar trend can be found in Figure 5 (f), with blood perfusion-induced heat loss being less in the heterogeneous case than in the homogeneous case. On the contrary, the difference in the magnitude of W_g between both cases increase up to 350 sec but gradually decreases afterward as time proceeds. This can be attributed to increasing differences between tissue temperature and blood tissue rather than reduced blood perfusion rates since the heat sink depends on the product of these two factors.

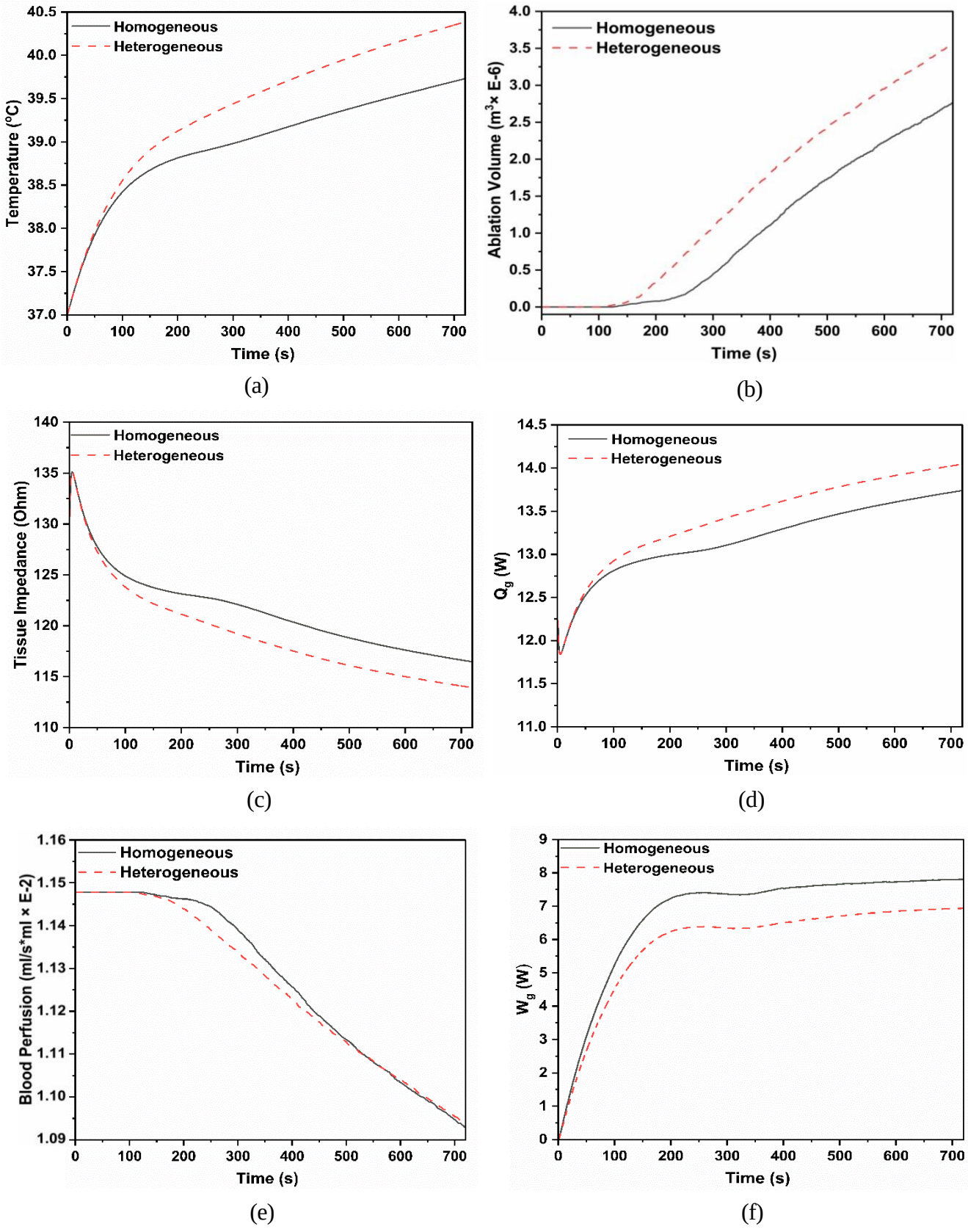

Figure 5. Time course plots of (a) Temperature, (b) Ablation volume, (c) Tissue impedance, (d) External heating source, (e) Blood perfusion, and (f) Heat loss due to blood perfusion for heterogeneous and homogeneous cases.

Shown in Figure 6 are the heating outcomes plotted as a function of the distance from the center of the RFA probe at the end of the treatment (720 sec). The variables are calculated for every voxel along a spherical surface described by the same distance of d_i, as schematically shown in Figure 6 (a). The tissue temperature increases gradually with the distance and peaks at 6 mm. This is because the probe cooling system continuously reduces the tissue temperature in the region near the probe. The temperature decreases to a lower level in the deep tumor tissue, mainly due to this region's low heating power. As a direct result, the ablation volume presents a similar non-linear relationship with the distance, with the largest volume of ablated tissue occurring at 10 mm from the probe. Moreover, comparisons show that the tissue temperature and thermal ablation volume are underestimated when the blood perfusion is assumed to be uniform across the tumor. The blood perfusion rate increases with the distance from the probe center in the homogeneous case. However, this monotonically increasing relationship does not exist because of the heterogeneous nature of blood perfusion *in vivo*.

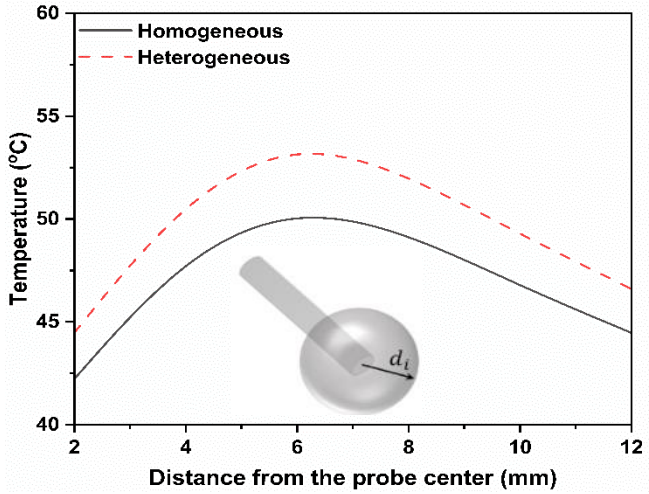

(a)

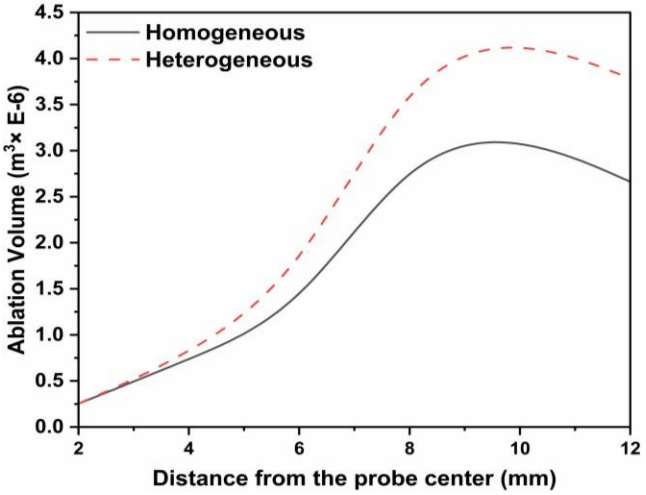

(b)

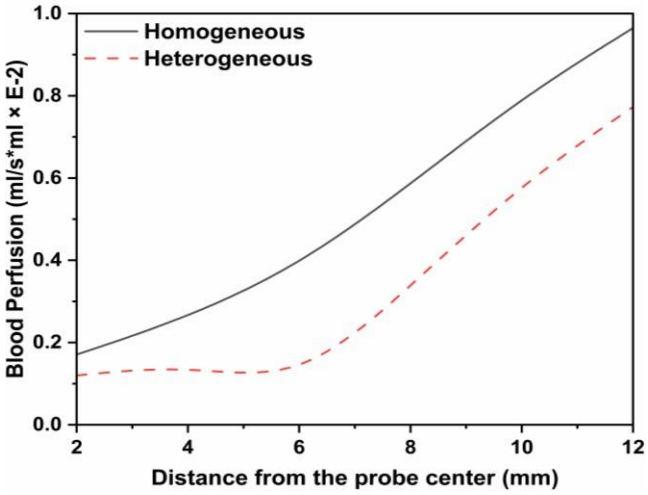

(c)

Figure 6. Distance course plots of (a) Temperature, (b) Ablation volume, and (c) Blood perfusion for heterogeneous and homogeneous cases.

In summary, these comparisons between the idealized homogeneous and realistic heterogeneous cases highlight the importance of using the realistic blood perfusion profile in the RFA modeling studies.

3.2 Impact of heating voltage

The heating voltage is a factor that can be precisely controlled in clinical practice. Numerous studies have used different voltage ranges and simulated the RFA treatment [14,39,40]. Therefore, a board range of 20V-90V is applied to study its impact on thermal ablation for the heterogeneous case, keeping the coolant temperature identical (10℃). Figure 7 compares the heating outcomes when different voltages are used. Unsurprisingly, the tissue temperature rises faster when higher power is used. However, the maximum tissue temperature is achieved when the voltage is 50V. This is mainly due to temperature control, determined by the tissue impedance. Results show that the heating at 20V-30V fails to trigger this control (Figure 7(c)), leading to a constant power supply and a continuous increase of tissue temperature over time (Figure 7(a)). Further increasing the heating power allows the impedance control to be activated; it would, in turn, effectively adjust the heating power to maintain the tissue temperature at similar levels of around 43℃. It is worth noting that the impedance control can only start functioning at the end of the 50V treatment, enabling the tissue to be continuously heated up to 46.5℃ in the first 650 seconds.

On the other hand, blood perfusion is significantly slowed down upon heating, as shown in Figure 7(e). A faster response can be found when the heating power is higher; however, the perfusion rate can decrease to a lower level in the 50V treatment due to more significant thermal damage. This would reduce the heat loss due to blood flow and maintain the tissue temperature. As the results illustrated in Figure 7(f), a relatively constant W_g can be found in the 50V treatment, although the tissue temperature shown in Figure 7(a) keeps increasing. Consequently, the most effective thermal ablation is achieved at 50V, as shown in Figure 7(b). It must be noted that the ablation volume in cases of 20 and 30 V remains negligible due to tissue temperature not being high enough to initiate thermal damage. This further leads to constant blood perfusion at these voltages.

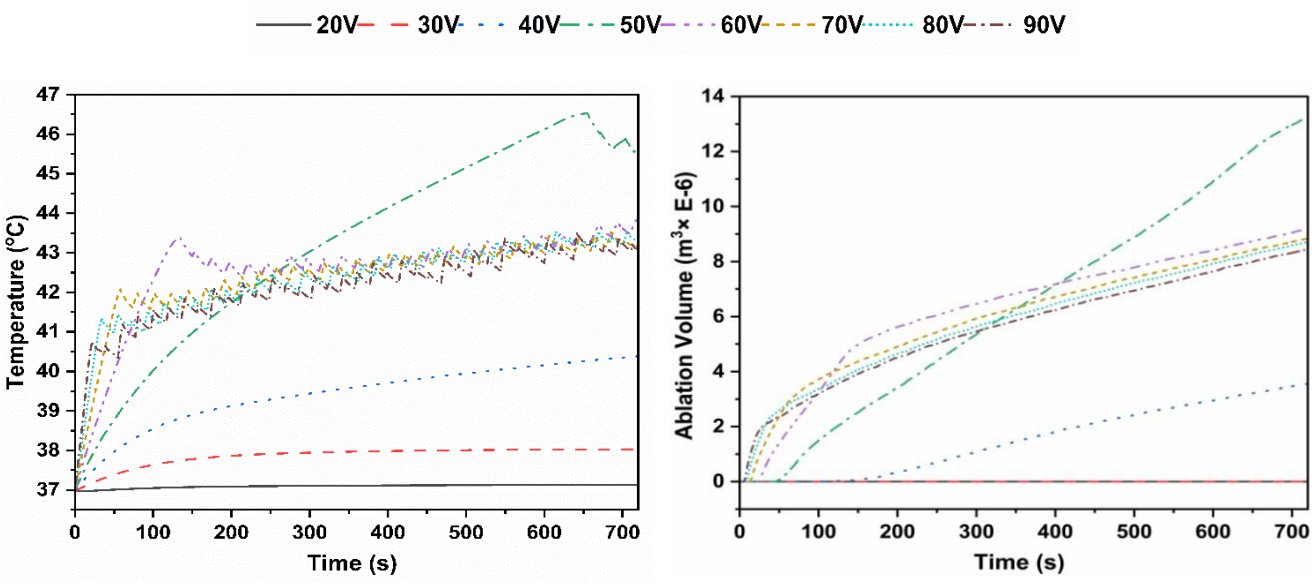

(a) (b)

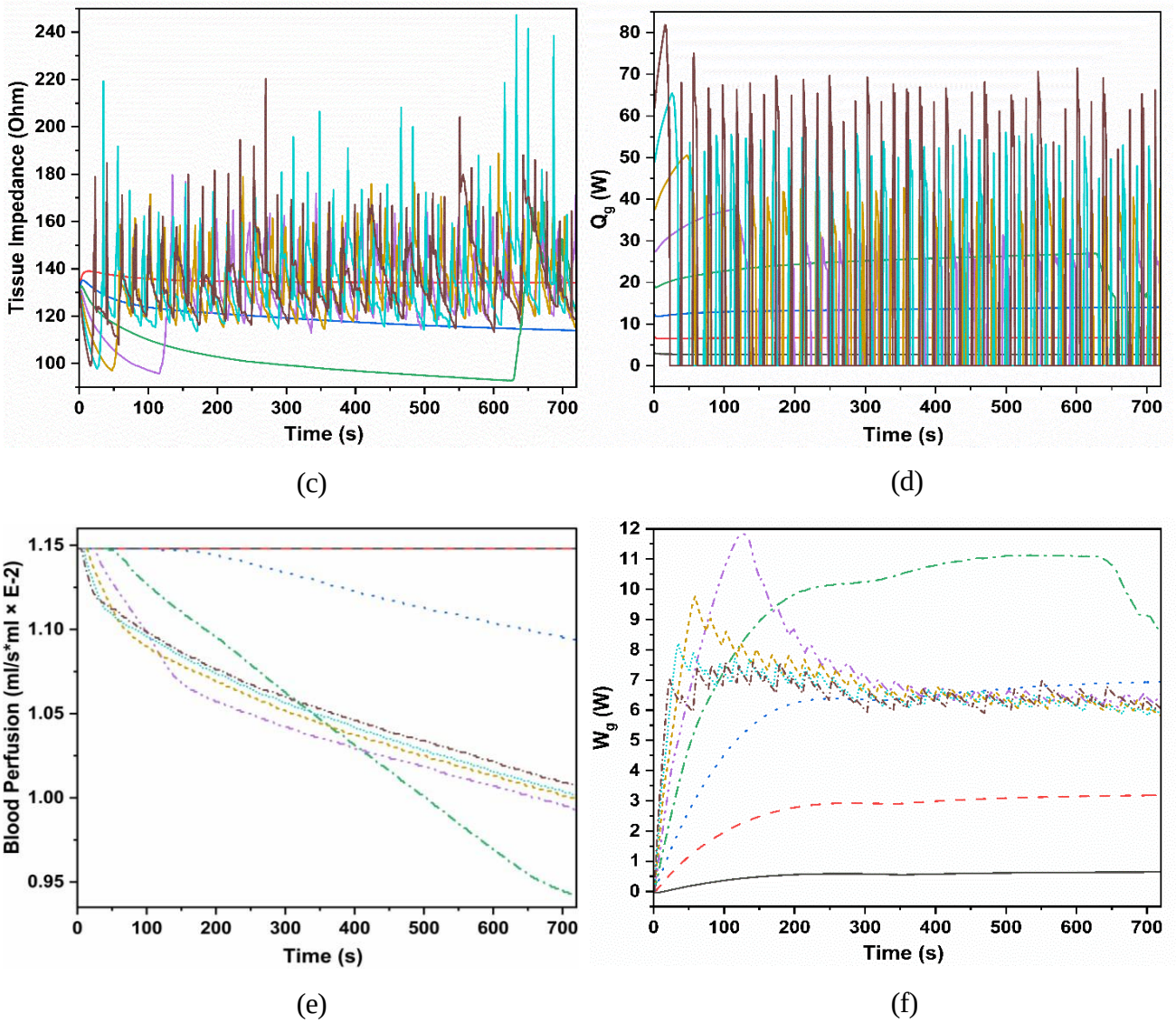

Figure 7. Time course plots of (a) Temperature, (b) Ablation volume, (c) Tissue impedance, (d) External heating source, (e) Blood perfusion, and (f) Heat loss due to blood perfusion for varying heating voltages.

The impacts of the voltage are further compared in the distance courses of heating outcomes in Figure 8. The tissue heating effect is poor when the power supply is in the range of 20V-30V. Therefore, the blood perfusion and tissue damage changes are insignificant and consistent with the time courses. Moreover, the heating power ranging from 50V-90V would result in similar temperature profiles. A slightly higher temperature can be found in the deep tissue when the voltage is 50V due to the reasons mentioned above, leading to slower blood perfusion and larger ablation volume in the deep tissue.

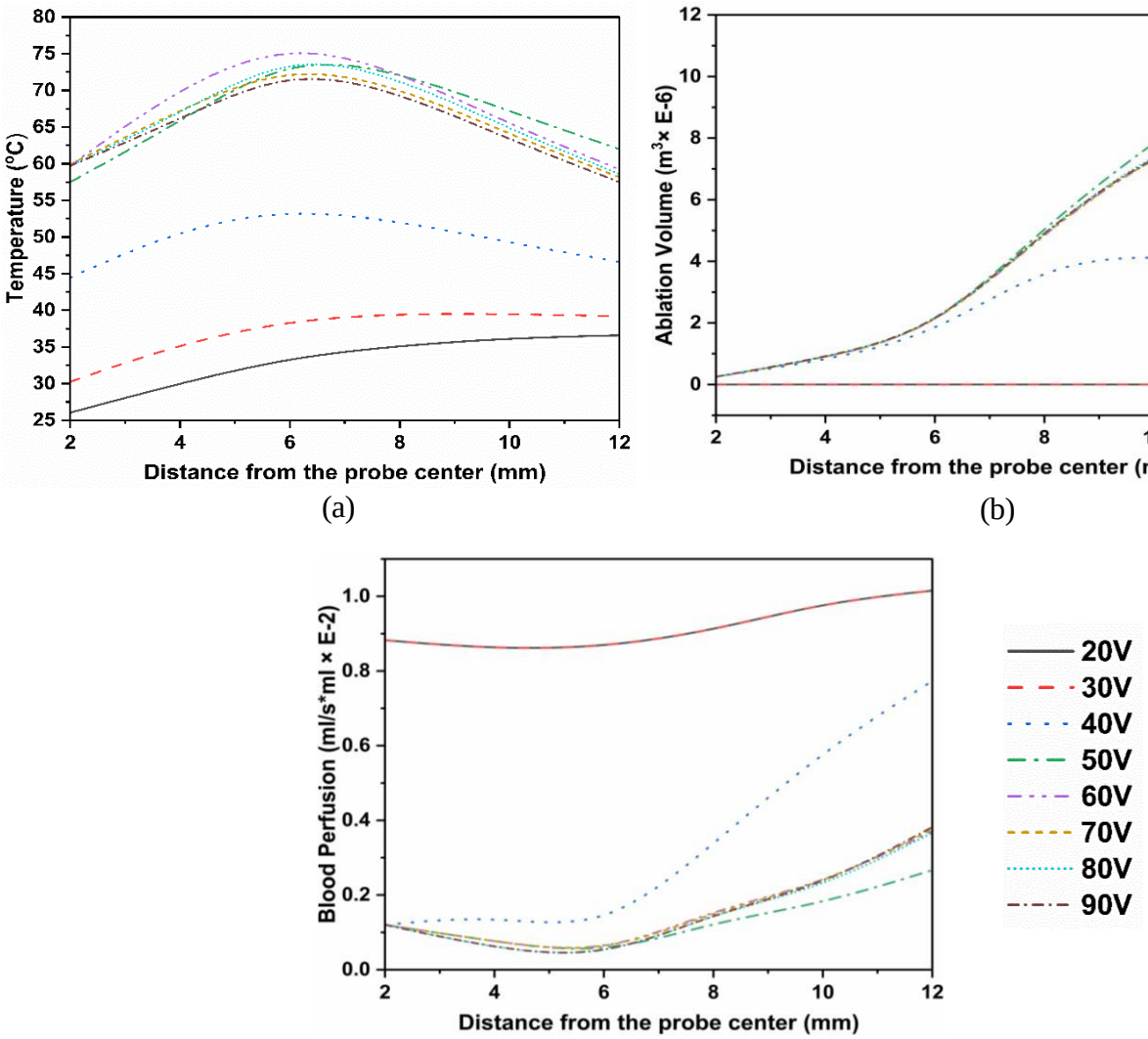

Figure 8. Distance course plots of (a) Temperature, (b) Ablation volume, and (c) Blood perfusion for varying heating voltages.

3.3 Impact of coolant temperature

The cooling system protects the probe from being overheated and damaged. The coolant runs through the inner portion of the probe, driven by a pump. It keeps the probe and the tissue next to it cool, providing reliable coagulation geometry and volume [41]. The coolant temperature is essential, ranging from 2℃ to 20℃ in practice [13,31,42]. Therefore, the same range is used in this study to examine its impact on the treatment. Two simulations are carried out at 40V and 50V, respectively. The results at the end of ablation show that the temperature distribution (Figure 9(a)) and the ablation volume (Figure 9(c)) are positively correlated with the coolant temperature when the heating power is supplied at 40V. Both of these parameters monotonically increase with the increase in the coolant temperature. More coagulation happens due to an increase in ablation volume leading to a monotonical decrease in blood perfusion (Figure 9 (e)). Nevertheless, the temperature control is yet triggered under this condition.

In contrast, the temperature control can be activated at 50V when the coolant temperature is 10℃ and above (Figure 9(b)). Although raising the coolant temperature enables the tissue temperature to increase faster, the temperature control can also be activated earlier to adjust the power supplied for heating. As a result, the tissue temperature is maintained at a relatively lower level, despite the faster reduction in blood perfusion (Figure 9(f)). A slightly higher ablation volume can be found when the coolant temperature is 10℃ (Figure 9(d)), indicating a non-linear relationship between the coolant temperature and thermal ablation. This differs from the treatment at 40V (Figure 9(c)). Tissue temperature and ablation volume are determined by the trade-off between the external heating source (dependent on tissue impedance) and heat loss due to blood perfusion, as explained in Section 3.2. The time course of these parameters for both the voltages and different coolant temperatures are represented in Figures C1(a)-(f) in Appendix C.

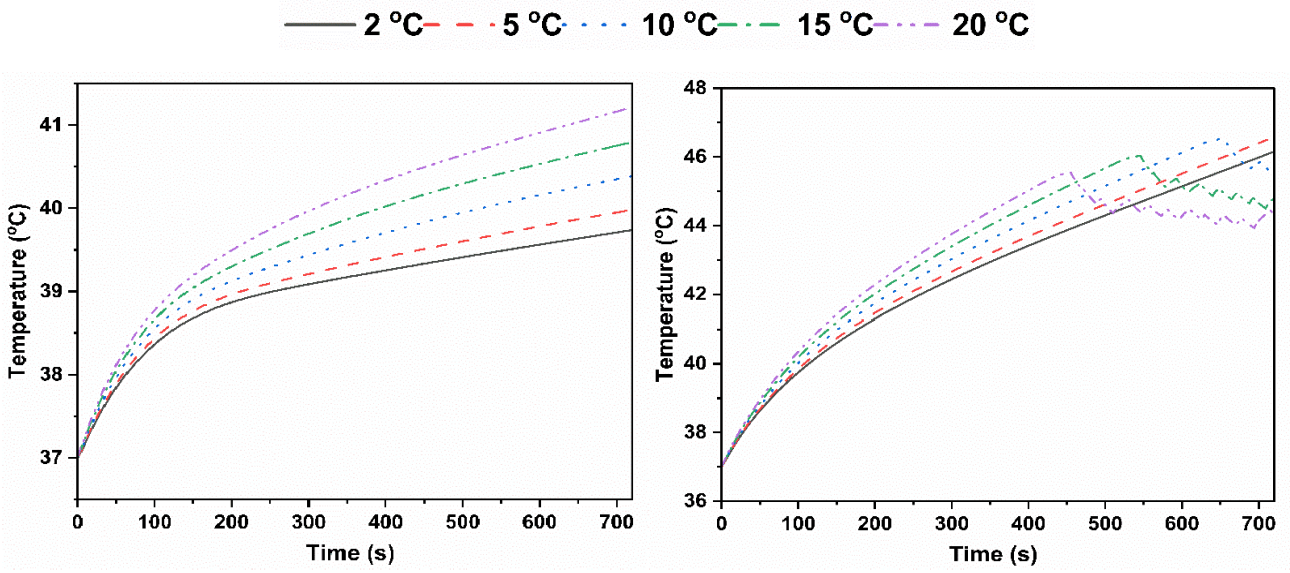

(a) (b)

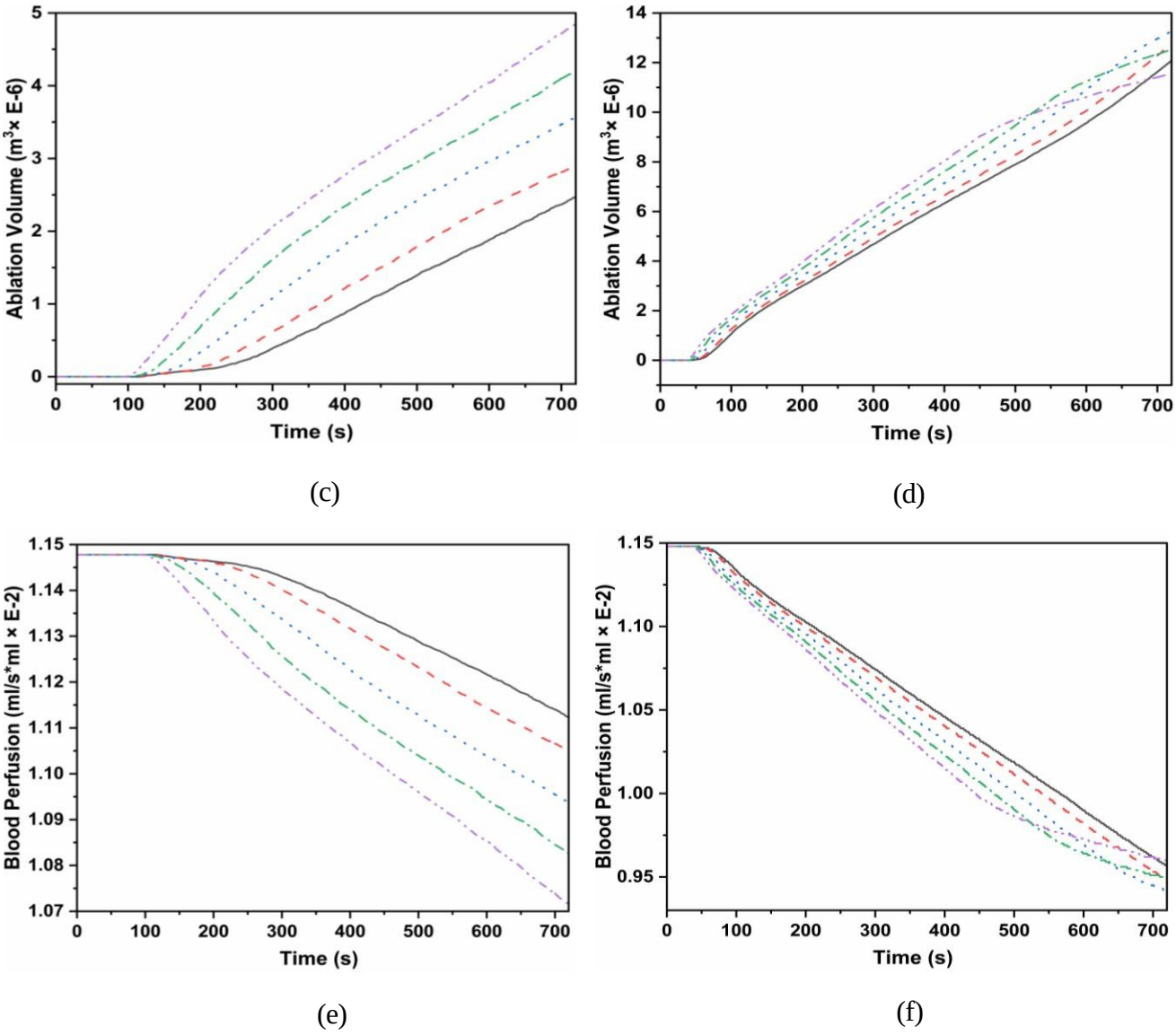

Figure 9. Time course plots of Temperature, Ablation volume and Blood perfusion for varying coolant temperatures at 40 V ((a), (c) and (e)) and at 50 V ((b), (d) and (f))

Figure 10 compares the 40V and 50V treatments regarding the distance courses of heating outcomes at the end of the treatment (720 seconds) for varying coolant temperatures. A positive relationship exists between the coolant temperature and the treatment effectiveness at 40V (Figures 10(a) and (c)). The best thermal damage is achieved at 20℃, the highest coolant temperature applied in practice. To be different, a slightly larger ablation volume of damaged tissue can be found when the coolant temperature is 10℃ in the 50V treatment (Figure 10(d)). However, the corresponding tissue temperature is not the highest when the treatment ends, as shown in Figure 10(b). The blood perfusion trends for both the voltages (Figures 10(e) and (f)) are self-explanatory and can be correlated with the corresponding ablation volume.

These comparisons between the treatments at 40V and 50V demonstrate that the coolant temperature cannot determine the thermal ablation alone; a dependence on the heating voltage exists, which is explained in the next section by examining their cross-impact.

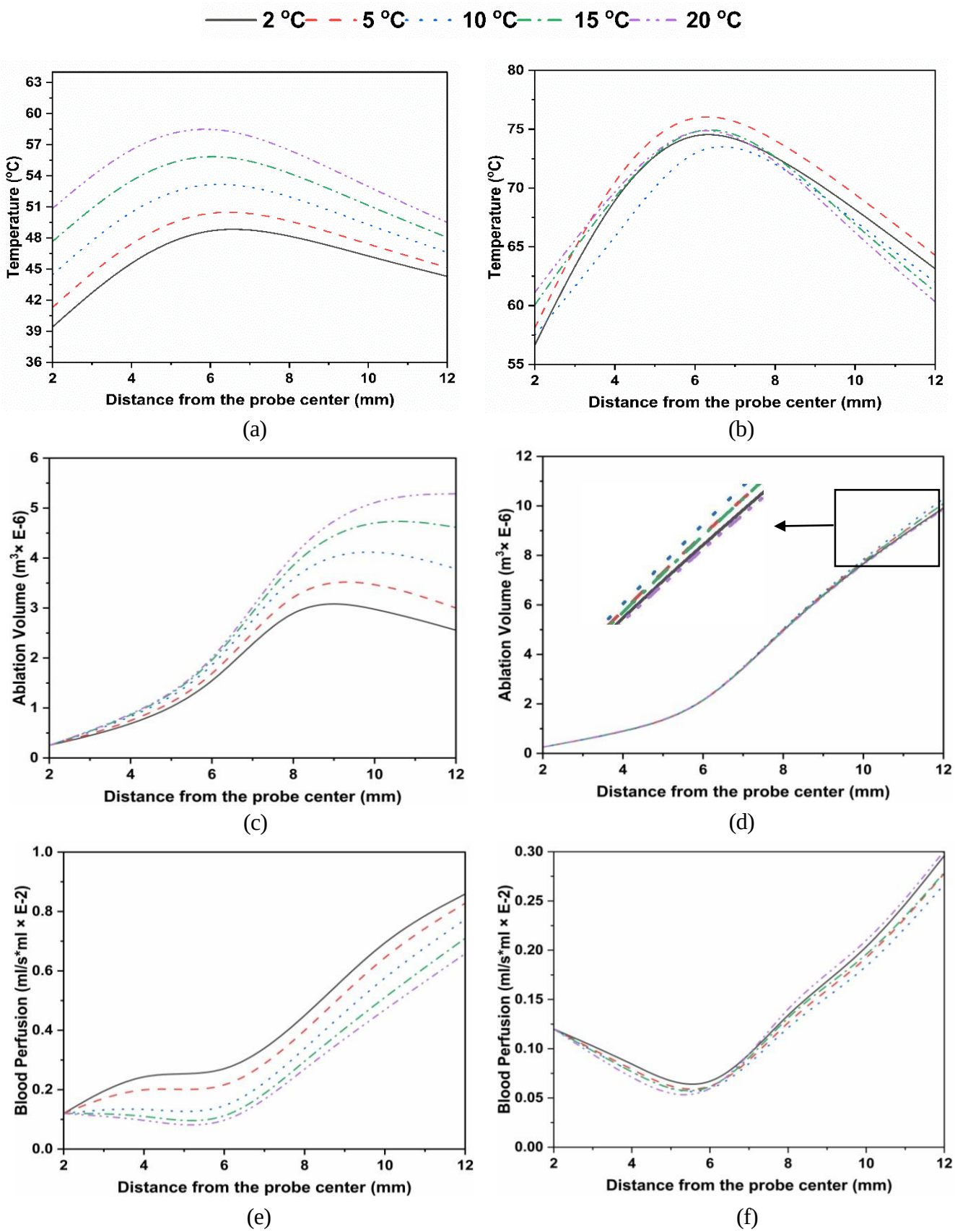

Figure 10. Distance course plots of Temperature, Ablation volume and Blood perfusion for varying coolant temperatures at 40 V ((a), (c) and (e)) and at 50 V ((b), (d) and (f))

3.4 Cross-impact of heating voltage and coolant temperature

The cross-impact of heating voltage and coolant temperature on the ablation volume for both cases is represented in Figure 11. Results show that $20V$ fails to lead to effective treatment. For treatment using $30V$, thermal damage can only be achieved when the coolant temperature is $20℃$ in the heterogeneous case; the ablation volume is $3.43 \times 10^{-8}m^3$. The thermal damage is non-linearly correlated to the voltage and coolant temperature in the case of heterogenous blood perfusion. The best treatment occurs at $50V$ and $10℃$ for the heating voltage and coolant temperature, respectively. Similar simulations are conducted under the assumption of homogeneous blood perfusion. Figure 11(b) shows the optimal heating condition in the homogeneous case is at 50V and 15 ℃.

In addition, it is observed that the ablation volume is underestimated in the homogeneous case for all the voltage and coolant temperature combinations. This difference further highlights the necessity to use heterogeneous blood perfusion in RFA modeling studies.

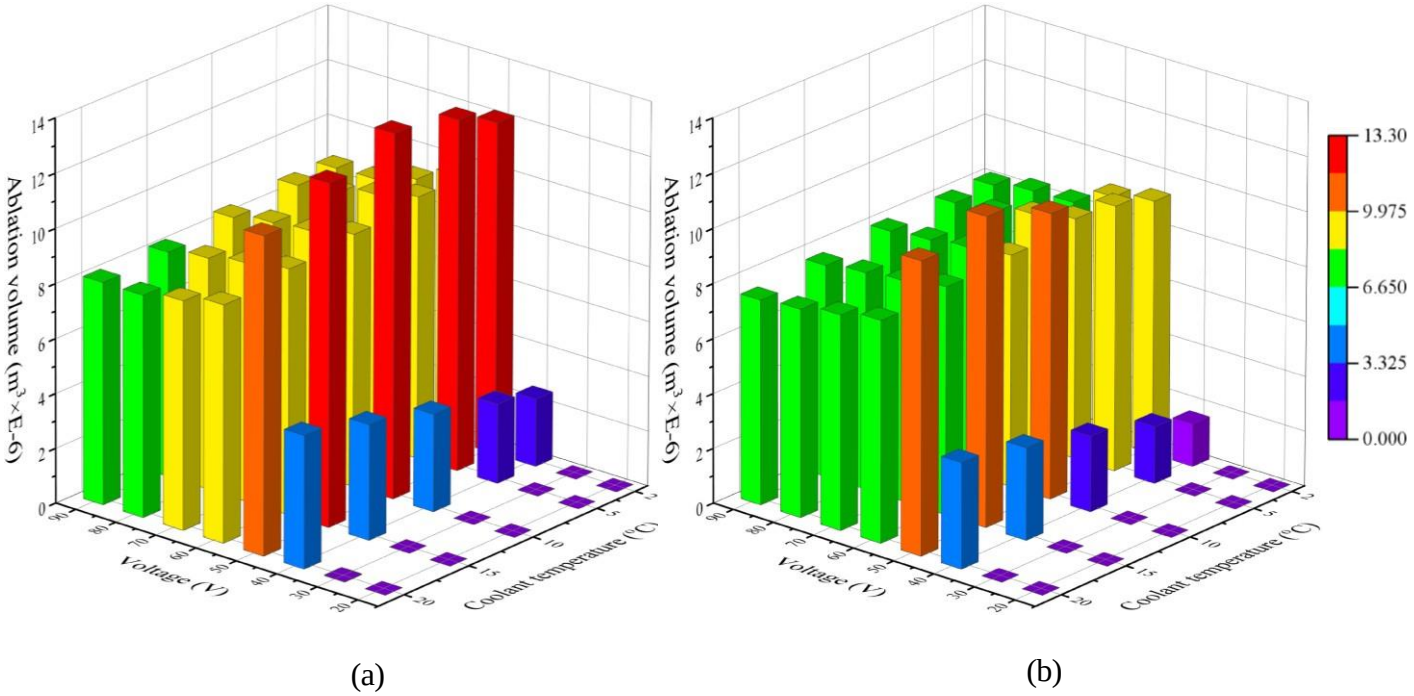

(a) (b)

Figure 11. Cross impact of voltage and coolant temperature on ablation volume at the end of the treatment (a) Heterogeneous and (b) Homogeneous

4. Discussion

The current study explores the effect of heterogeneous blood perfusion on the therapeutic efficacy of RFA treatment, in contrast to previous modeling studies where homogeneous blood perfusion was assumed throughout the tissue. For this endeavor, heterogeneous perfusion is extracted from DCE-MRI data and incorporated into the computational model voxel-wise. The simulated results demonstrate that blood perfusion strongly affects the temperature distribution and ablation volume, which can be underestimated in homogeneous cases. In practice, the

blood perfusion may vary among patients; thus, the voltage required to achieve tissue necrosis, time to reach the target temperature, and optimal treatment time are bound to change. In this regard, the RFA treatment parameters must be tuned individually based on patients' blood perfusion to get the optimum therapeutic outcome.

In the current study, an impedance-controlled pulsing protocol is used to avoid tissue charring, consistent with the clinical practice of RFA treatment where the same control has been used. Moreover, another method named temperature-controlled RFA is also commonly employed. This feedback control system has been modeled in previous theoretical studies on RFA, where the temperature at the probe tip is controlled by a PID controller [11]. This control mechanism is based on a closed-loop system that calculates the error between the target and current probe tip temperature to modulate the input voltage accordingly. Nevertheless, the measured probe tip temperature does not accurately represent the tissue temperature; therefore, impedance-based switching is preferred [14,43]. It must be noted that the impedance threshold value and the roll-off time may vary depending on the application, which can result in changes in the ablation volume [44]. Furthermore, the cut-off value and the roll-off time may differ among patients due to the individual difference in blood perfusion. In the future, a sensitivity study can be carried out to optimize these parameters for different patients to maximize therapeutic efficiency.

In addition to the Arrhenius model, the theoretical models of isotherm contour [45] and TID [46] have also been developed to evaluate tissue necrosis in RFA treatment. However, both applications are subject to certain limitations. Isotherm contour uses a fixed tissue temperature of 50℃ to evaluate tissue death, which can lead to an overestimation of the ablation volume as it highly depends on ablation time and target tissue [43]. Similarly, the TID model evaluates ablation in terms of CEM by setting the reference temperature as 43℃. Tissues with a CEM in the range of 120-240 minutes were considered dead. However, this method becomes inapplicable when the tissue temperatures exceed 50 ℃, thus limiting its use [46]. In place of this, the Arrhenius model is the most optimum to predict thermal damage in the numerical modeling of RFA studies.

Different relationships between the temperature dependence of electrical and thermal conductivities have been developed in previous modeling studies. In addition to the linear correlation used in the current study, an exponential function of electrical conductivity has also been applied [13–15]. However, studies demonstrated that the predicted ablation zone is less influenced by choice of this relationship [47]. Similarly, different algorithms were implemented for the temperature dependence of blood perfusion; their comparative impact on the ablation zone size was studied [20]. An insignificant change in the dimensions of the ablation zone was reported when an increase in blood perfusion was included for a low degree of statis case while solving the first-order Arrhenius equation.

Pennes' bioheat equation has been used in the current study to model the temperature distribution inside the tissue due to its simplicity. However, since the tumor tissue is treated as a porous medium, bioheat equations established on porous media theory can also be applied to

provide more accurate predictions of tissue temperature and thermal damage [48]. This will thus reduce assumptions and, in particular, enable explicitly predicting blood and tissue temperature while considering the direction of blood flow. The superiority of porous media equations over Pennes' bioheat equation has been demonstrated in the simulations of the RFA treatment against liver tumors [49]. The current study uses heterogeneous blood perfusion at each tumor tissue voxel, relaxing the uniform perfusion assumption. Future studies can be carried out to model RFA using porous media equations by collectively incorporating the porosity and blood perfusion information extracted from DCE-MRI [50,51]. This will improve the modeling of the RFA treatment of tumors.

The present study involves several assumptions and limitations that can be explored in the future. First, the model validation in the current work is against an *ex vivo* experimental study without considering blood perfusion. Since the present study is focused on the importance of patient-specific heterogenous blood perfusion, a thorough quantitative validation of the predicted results is cumbersome due to the lack of such experimental data. However, a model validation against an *in vivo* experimental study can improve the accuracy and robustness of the developed model. Second, the simulations have been performed using a single monopolar RFA probe. Consequently, the heating region is highly localized, limiting the ablation zone and thermal damage, as shown in distance courses (Figure 5(a)-(c)). In practice, multiple RFA/cluster probes [19] or multi-tined RFA probes [15] are commonly employed to enlarge the ablation zone and enhance therapeutic efficacy [43]. Moreover, bipolar RFA probes are also recommended to enhance the coagulation volume [13]. In this regard, the usage of multiple RFA probes, their switching protocol, operating mode, and the probe arrangement inside the heterogeneously perfused tissue is worthy of in-depth study in the future. Third, the RFA probe has been inserted in the center of the tumor perpendicular to the XY plane. However, the probe can be placed in a pre-selected position and an optimized posture. This should be carefully considered in practice, as inaccurate probe placement is one of the main challenges in the RFA procedure [43]. In the future, an optimization study can be carried out to investigate the effect of probe positioning in higher or lower-perfused regions of the tissue to maximize the thermal damage. Fourth, the convective heat transfer coefficient was kept identical while changing the coolant temperature. This is based on the assumption of the same flow rate in all the cases due to the lack of experimental data. Fifth, the electrode geometry has been taken to be square rather than cylindrical, ignoring the conical tip commonly employed in previous studies [12,35]. This is because the square shape probe is easy to mesh in line with the voxelized methodology, which further satisfies the need for a one-to-one mapping of blood perfusion data from DCE-MRI to CFD. The importance of the voxelized methodology has been explained in our previous studies [50–52]. Furthermore, recent studies report that the numerical results do not vary significantly whether or not the conical tip is considered [42]. Since the study aims to highlight the importance of blood perfusion heterogeneity, the relative changes in treatment outcomes between the heterogeneous case and homogeneous case will not change much with the probe geometry. Last, the values of the parameters such as density, specific heat capacity, and thermal conductivity (summarized in Table 1) have been assumed to remain the same in normal and tumor tissues, in line with the previous studies [13,53]. This is because the RF heating is highly localized, as shown in Figure 4, the thermal effect on normal tissue can be

neglected. It is worth mentioning that the values of these model parameters would change depending on the tissue type. Representative values of model parameters are taken due to the data availability, which would not affect the qualitative nature of the results. Tissue-specific parameters can be incorporated to enhance the quantitative accuracy of the results in the future. Their impact can also be examined in the following study. In summary, results obtained from this study can only be used for qualitative comparison to identify the opportunities for improving the RFA treatment. Results must be further evaluated against data from both *ex vivo* and *in vivo* experiments before providing guidelines to clinicians and surgeons for developing the treatment plan.

5. Conclusions

In this study, an image-based computational model is developed to simulate RFA in human brain tumors by using the heterogeneous blood perfusion values extracted from DCE-MRI data. Comparisons with the homogeneous case demonstrate the importance of blood perfusion heterogeneity in estimating the tissue temperature and ablation volume since the treatment outcome can be underestimated when uniform perfusion is used. Moreover, the heat can penetrate deeper into the tissue with the heterogenous blood perfusion, thereby enlarging the ablation zone. The *in-silico* results also suggest that due to the patient-specific nature of blood perfusion, the clinical settings of RFA parameters must be tailored for each patient to maximize the therapeutic output. To demonstrate it, commonly used RFA parameters such as voltage and coolant temperature were optimized for two different patients. This study highlights the need to incorporate blood perfusion heterogeneity in future RFA modeling studies. The results shown in the current study may serve as a reference for clinicians and surgeons to develop new optimal patient-specific clinical protocols and systems for RFA applications.

Funding: Ajay Bhandari would like to acknowledge the support received by a grant from the Science and Engineering Research Board (Grant Number: SRG/2021/000053). Wenbo Zhan acknowledges the support received from the Royal Society of Edinburgh (Grant Number: SAPHIRE-2999). Both authors would like to acknowledge the support received from the Royal Society (Grant Number: IES\R1\221015). Anup Singh acknowledges the support received from Science and Engineering Research Board (Grant Number: CRG/2019/005032)

Data Availability Statement: The data supporting this study's findings are available from the corresponding author upon reasonable request.

Acknowledgments: The authors thank Dr. RK Gupta (Director Radiology, Fortis Memorial Research Institute, Gurugram, India) for providing the clinical DCE-MRI data of human brain tumors.

Conflicts of Interest: The authors declare no conflict of interest.

Appendix A

The grid independence has been performed by disseminating each mesh element into four quadrants using a similar strategy described in the previous study [22]. The respective quadrant is assigned the same blood perfusion value and model parameters as the parent voxel. An illustration of the grid independency for the heterogeneous case of the baseline study is shown in Figures A1 and A2. The time course and distance course of tissue temperature and ablation volume have been plotted for the computational meshes with different numbers of elements. Significant changes in the average tissue temperature (Figure A1(a) and Figure A2(a)) and ablation volume (Figure A1(b) and Figure A2(b)) can be observed between the original mesh (82944 elements) and the mesh which is four times finer (331776 elements).

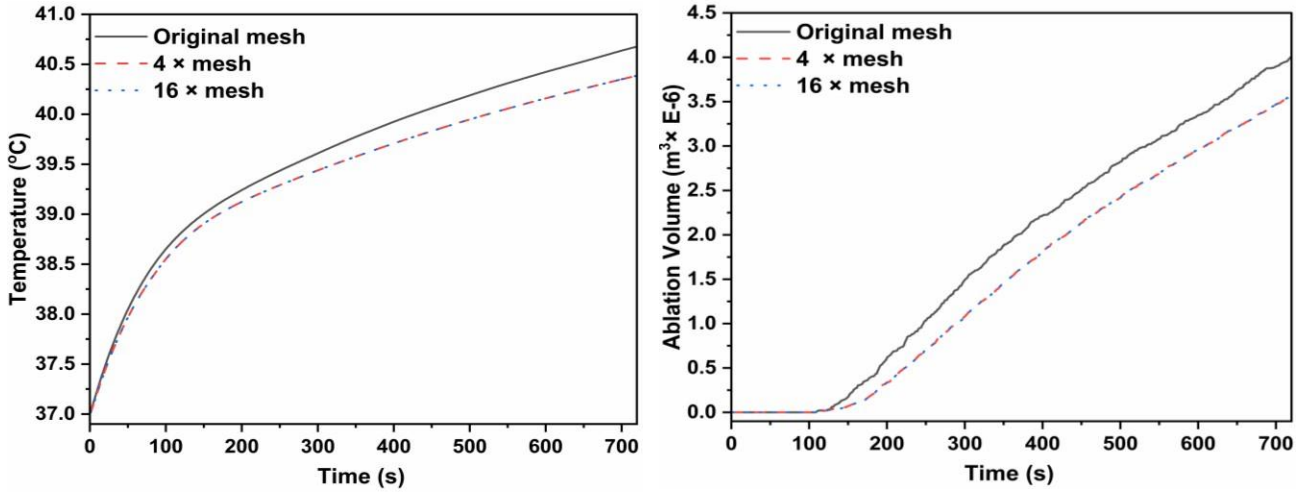

(a) (b)

Figure A1. Time course plots of (a) Temperature, and (b) Ablation volume for different mesh elements

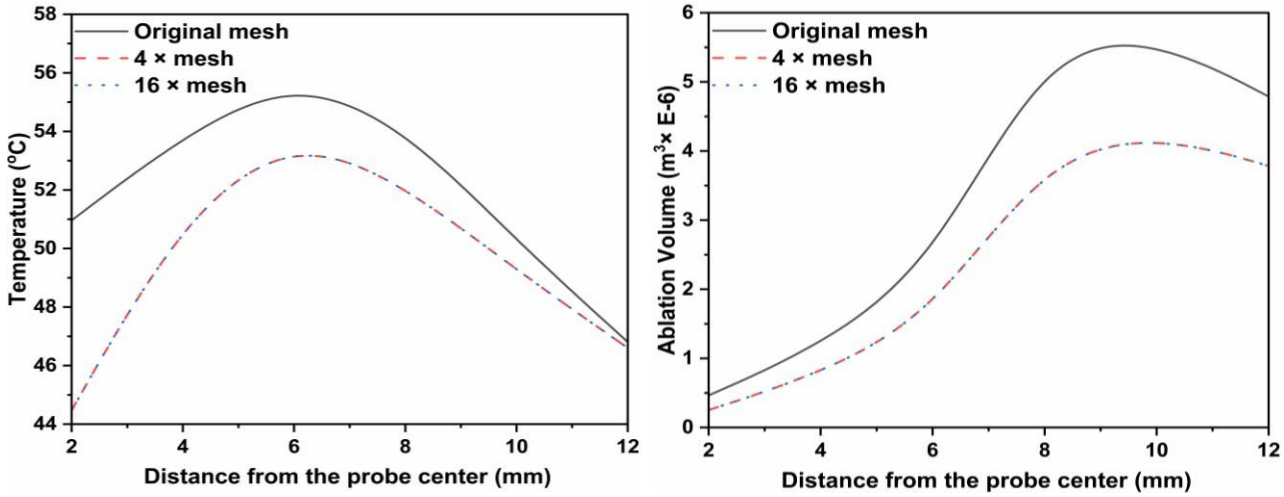

(a) (b)

Figure A2. Distance course plots of (a) Temperature, and (b) Ablation volume for different mesh elements.

Therefore, the mesh is further refined to sixteen times the original mesh (1327104 elements), adopting a similar strategy of parameter allocation. The temperature and ablation volume changes are neglectable between the mesh with 331776 and 1327104 elements. Therefore, the computational mesh consisting of 331776 elements is applied in the current study. This is for the simulation using Patient 1's data. A similar grid independence study is performed for Patient 2, with the final mesh consisting of 134064 elements.

Appendix B

This section shows simulation results for Patient 2. The mathematical model, extraction of blood perfusion from DCE-MRI data, model parameters, and numerical methodology are kept the same as in the simulation using Patient 1's data. Results shown in the following sections support the conclusions.

Appendix B.1 Tumor geometry and heterogeneous blood perfusion properties

The geometry and the perfusion parameters of Patient 2's tumor are extracted using the same procedure mentioned in Section 2.2. The blood perfusion contours of all the slices, along with the pre-and post-contrast images, are shown in Figure B1

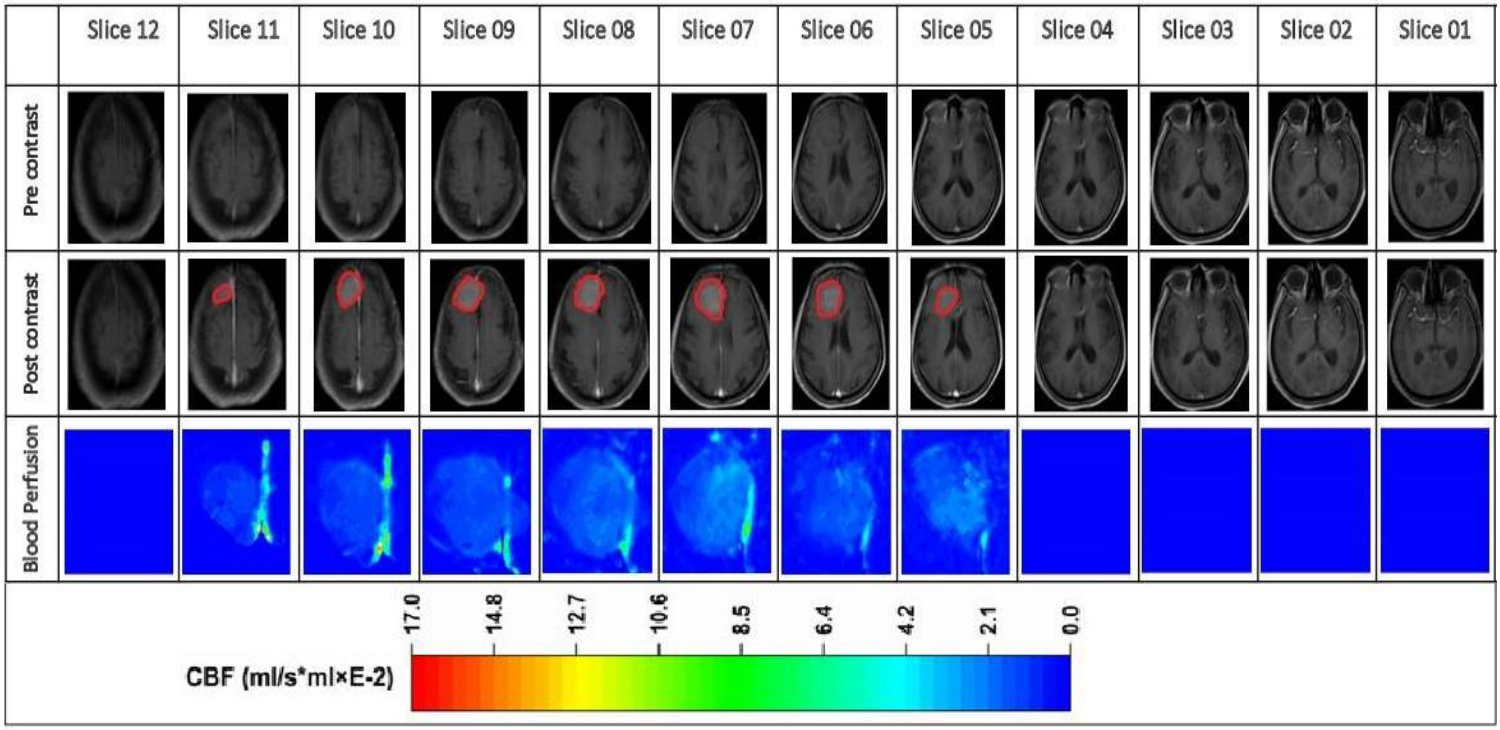

Figure B1. Tissue heterogeneous properties extracted from patient DCE-MR images. The interface between the brain tumor and its holding tissue is marked in red in the post-contrast images.

Appendix B.2 Baseline study (Effect of blood perfusion heterogeneity)

The RFA treatment for Patient 2 is simulated with the RF voltage and coolant temperature set to 40V and 10℃, respectively. The predicted tissue temperature and ablation volume time courses are compared between the heterogeneous and homogeneous cases in Figure B2(a) and (b), respectively. Results show that assuming the uniform blood-perfusion rate would lead to underestimating the heating outcomes and RFA effectiveness. Similar results can also be found for the distance courses shown in Figure B3. These findings agree with those obtained using Patient 1 data.

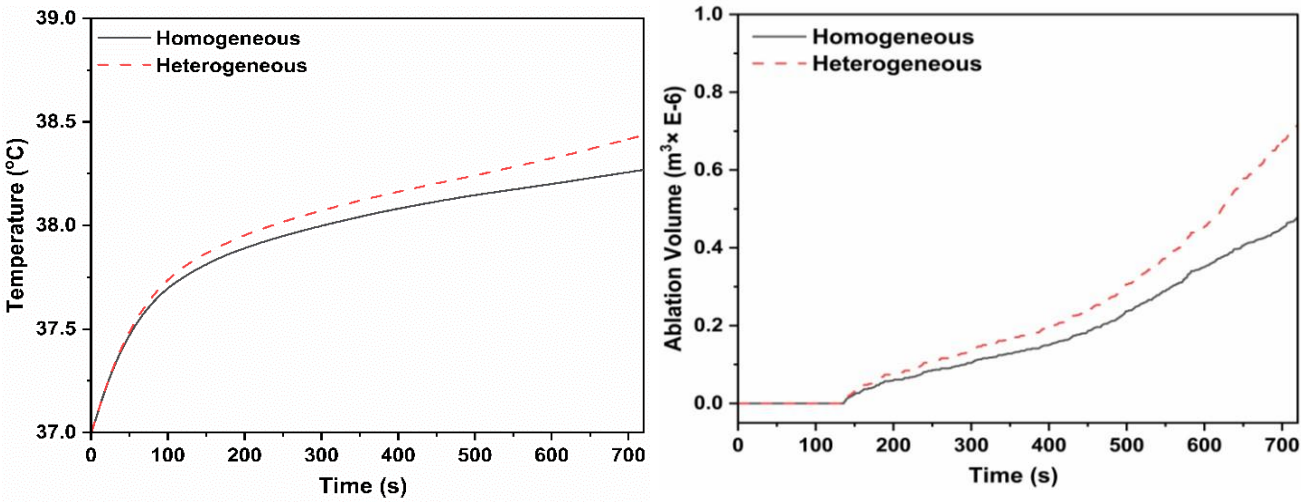

(a) (b)

Figure B2. Time course plots of (a) Temperature, and (b) Ablation volume for heterogeneous and homogeneous cases.

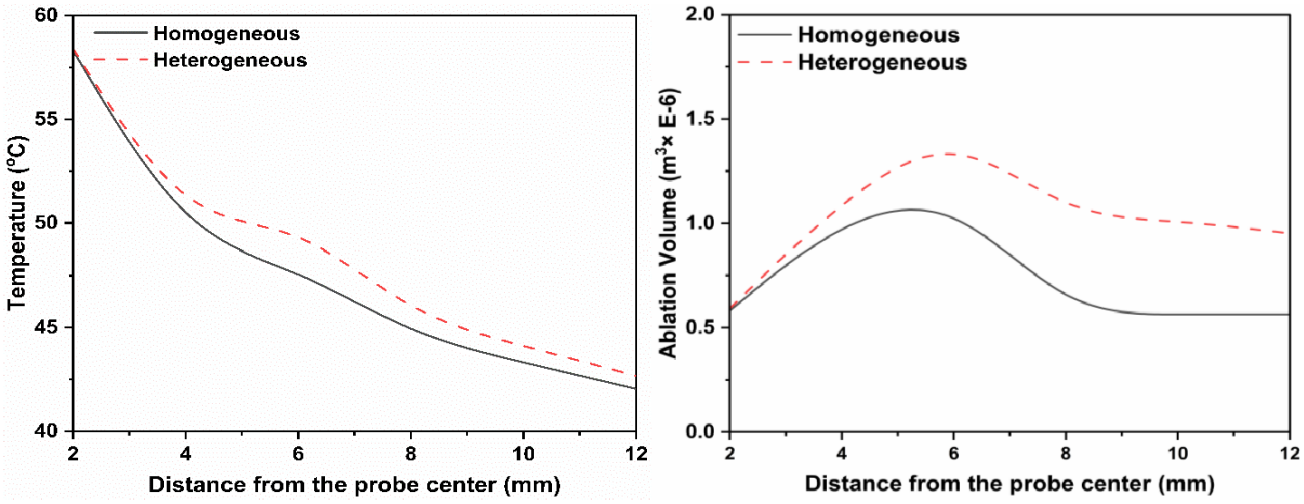

(a) (b)

Figure B3. Distance course plots of (a) Temperature, and (b) Ablation volume for heterogeneous and homogeneous cases.

Appendix B.3 Impact of heating voltage

The impact of RF voltage on the heating outcomes is further examined using Patient 2's data. The coolant temperature is set at 10℃ in all the simulated treatments. Results in Figure B4 show that setting the voltage to 60V and above can trigger the temperature controller successfully. Although a high heating voltage increases tissue temperature and ablation volume, the increase is significantly slowed down after the temperature control is activated. On the contrary, the temperature control remains off throughout the treatment when the voltage is 50V and below. Therefore, the tissue temperature increases continuously. The highest tissue temperature of 41.5℃ occurs when the heating voltage is 50V. Comparable ablation volumes can be found for 50V ($3.80 \times 10^{-6}m^3$) and 60V ($3.24 \times 10^{-6}m^3$) at 720 seconds, with a slightly larger volume achieved in the 50V treatment.

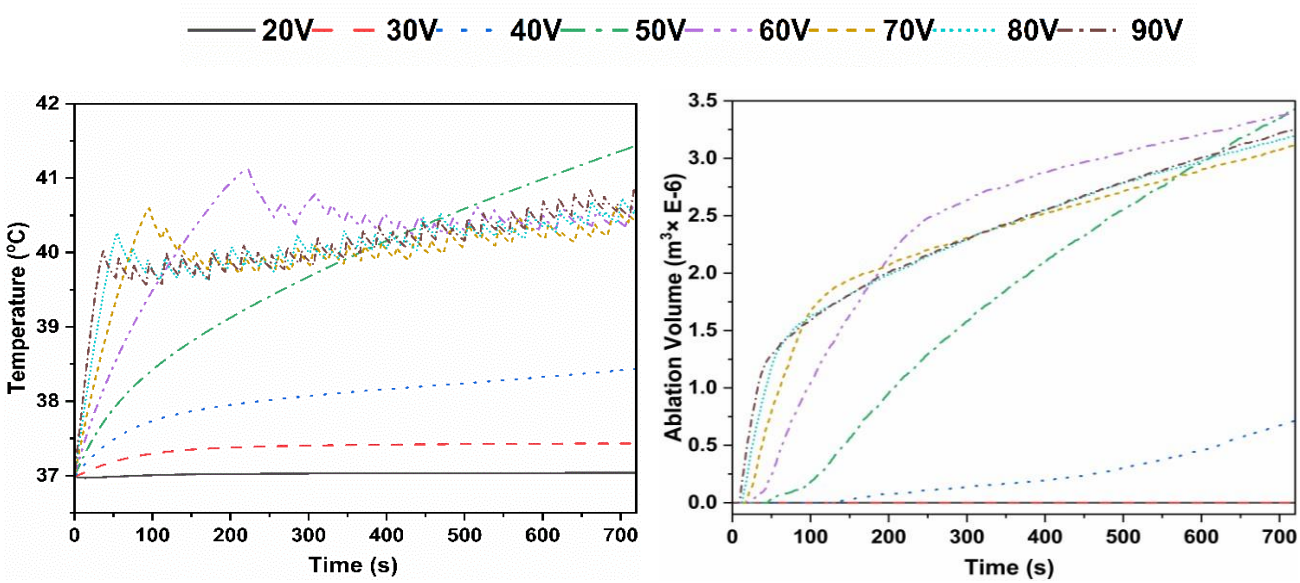

(a) (b)

Figure B4. Time course plots of (a) Temperature, and (b) Ablation volume for varying heating voltages.

Appendix B.4 Impact of coolant temperature

The impact of coolant temperature is studied using Patient 2's data in two simulations in which the RF voltage is set to 40V and 50V, respectively. The heating outcomes are summarised in Figure B5. Since these voltages are not high enough to activate the temperature controller, as shown in Figure B4, the tissue temperature and ablation volume are positively correlated to the coolant temperature. This is consistent with the findings for Patient 1, as represented in Figure 9.

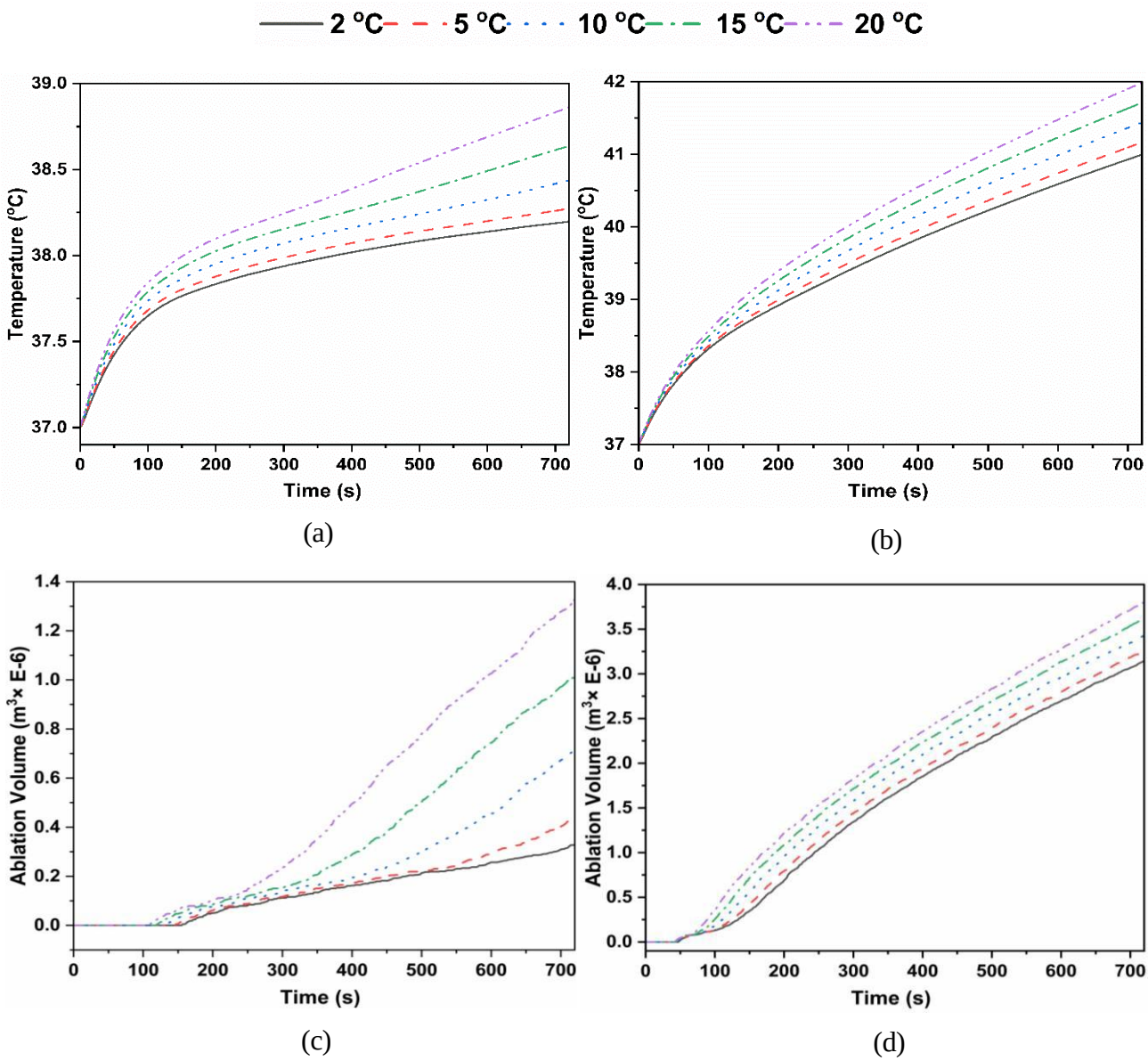

Figure B5. Time course plots of Temperature, and Ablation volume for varying coolant temperatures at 40 V ((a), (c)) and at 50 V ((b), (d))

Appendix B.5 Cross impact of heating voltage and coolant temperature

For patient 2, the highest ablation volume occurs at 50V and 20 ℃ for the heating voltage and coolant temperature, respectively, in the case of heterogenous blood perfusion (Figure B6(a)). Additionally, the same optimal heating conditions were optimum for the homogeneous case, which is different compared to Patient 1. However, for all the combinations, the ablation volume in the homogeneous case is underestimated (Figure B6(b)), which is in line with Patient 1 results.

All the aforementioned analyses show that blood perfusion heterogeneity is patient and location-specific. It can significantly change the ablation outcomes and the optimal selection of RFA treatment parameters for a particular patient.

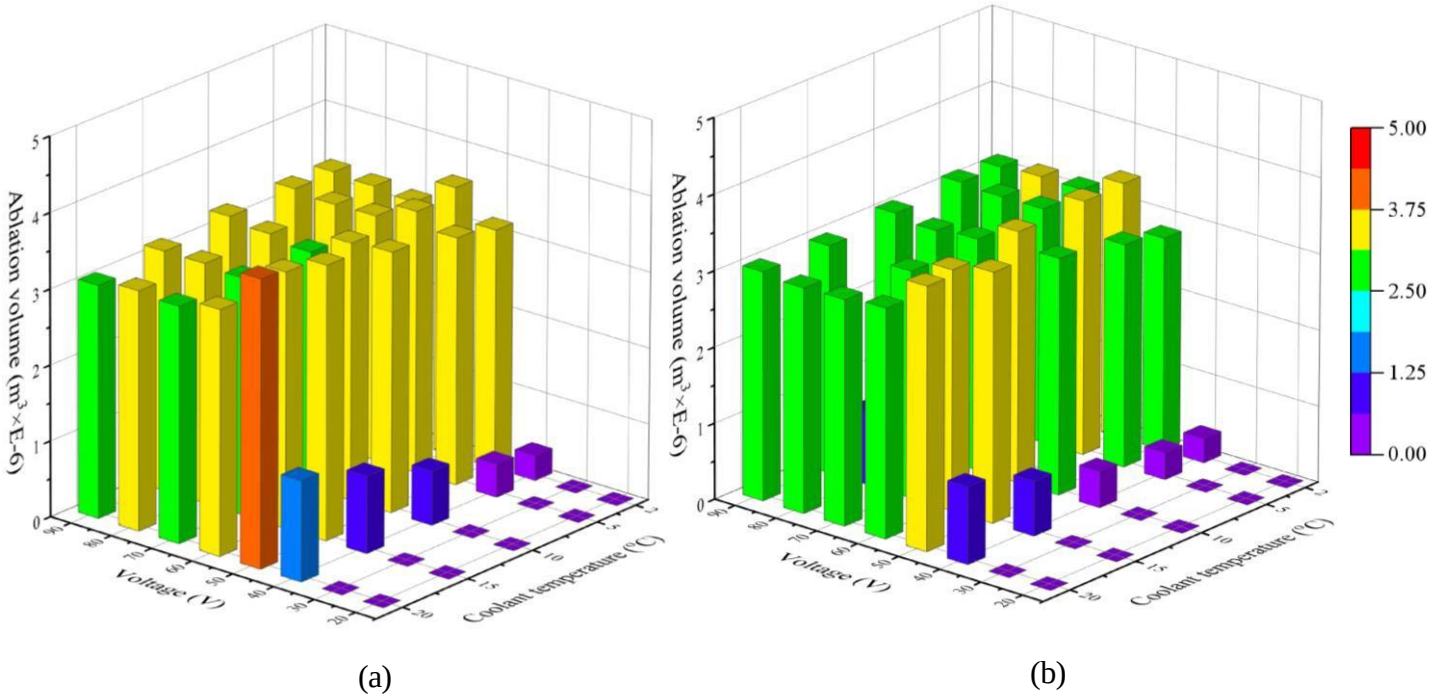

(a) (b)

Figure B6. Cross impact of voltage and coolant temperature on ablation volume at the end of the treatment (a) Heterogeneous and (b) Homogeneous

Appendix C:

The impact of cooling temperature on tissue impedance, Q_g, and W_g for 40V and 50V is shown in Figure C1. It can be observed that Q_g increases monotonously with an increase in coolant temperature (Figure C1(c)) at 40V due to a monotonous decrease in tissue impedance (Figure C1(a)). Further, W_g also increases (Figure C1(e)); however, the magnitude of Q_g being more significant than W_g leads to an increase in tissue temperature (Figure 9 (a)) and ablation volume (Figure 9 (c)). At 50V, since temperature control is triggered at 10℃, tissue impedance (Figure C1(b)) shoots, leading to a drop in Q_g ((Figure C1(d))). Further, with an increase in coolant temperature at 50V, the trigger is initiated early, leading to a faster drop in Q_g and W_g , which leads to a quicker reduction in temperature (Figure 9 (b)) and ablation volume (Figure 9 (d)).

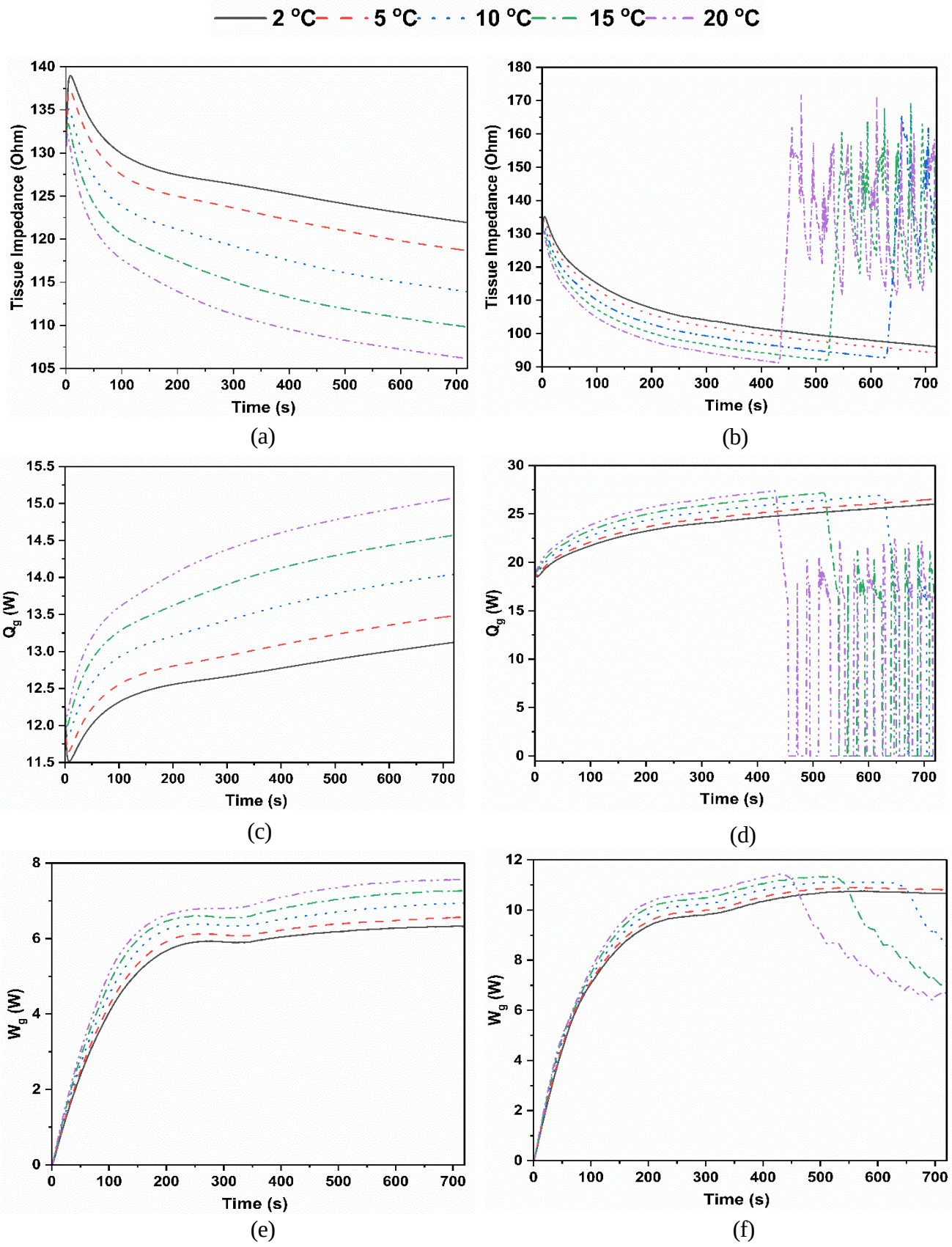

Figure C1. Time course plots of tissue impedance, external heating source and heat loss due to blood perfusion at 40 V ((a), (c) and (e)) and at 50 V ((b), (d) and (f))

References:

[1] S. McDermott, D.A. Gervais, Radiofrequency ablation of liver tumors., Semin. Intervent. Radiol. 30 (2013) 49–55. https://doi.org/10.1055/s-0033-1333653.

[2] Y. Anzai, R. Lufkin, A. De Salles, K. Farahani, A. Huang, S. Sinha, E. Behnke, K. Black, Radiofrequency ablation of brain tumours using MR guidance, Minim. Invasive Ther. Allied Technol. 5 (1996) 232–242. https://doi.org/10.3109/13645709609153297.

[3] R.J. Gillies, P.A. Schornack, T.W. Secomb, N. Raghunand, Causes and effects of heterogeneous perfusion in tumors, Neoplasia. 1 (1999) 197–207. https://doi.org/10.1038/sj.neo.7900037.

[4] D. Haemmerich, J.G. Webster, Automatic control of finite element models for temperature-controlled radiofrequency ablation, Biomed. Eng. Online. 4 (2005) 1–8. https://doi.org/10.1186/1475-925X-4-42.

[5] I. Altrogge, T. Preusser, T. Kröger, C. Büskens, P.L. Pereira, D. Schmidt, H.O. Peitgen, Multiscale optimization of the probe placement for radiofrequency ablation, Acad. Radiol. 14 (2007) 1310–1324. https://doi.org/10.1016/j.acra.2007.07.016.

[6] C.C.R. Chen, M.I. Miga, R.L. Galloway, Optimizing electrode placement using finite-element models in radiofrequency ablation treatment planning, IEEE Trans. Biomed. Eng. 56 (2009) 237–245. https://doi.org/10.1109/TBME.2008.2010383.

[7] L. Xu, K. Cai, R. Yang, Q. Lin, H. Yue, F. Liu, Simulation of multi-probe radiofrequency ablation guided by optical surgery navigation system under different active modes, Comput. Assist. Surg. 21 (2016) 107–116. https://doi.org/10.1080/24699322.2016.1210679.

[8] M. Trujillo, J. Bon, M.J. Rivera, F. Burdío, Computer modelling of an impedance-controlled pulsing protocol for RF tumour ablation with a cooled electrode, 6736 (2016) 931–939. https://doi.org/10.1080/02656736.2016.1190868.

[9] A.S.K. Kho, J.J. Foo, E.T. Ooi, E.H. Ooi, Shape-shifting thermal coagulation zone during saline-infused radiofrequency ablation : A computational study on the effects of different infusion location, Comput. Methods Programs Biomed. 184 (2020) 105289. https://doi.org/10.1016/j.cmpb.2019.105289.

[10] J.J. Pérez, A. González-suárez, E. Nadal, E. Berjano, Thermal impact of replacing constant voltage by low-frequency sine wave voltage in RF ablation computer modeling, Comput. Methods Programs Biomed. 195 (2020) 1–7. https://doi.org/10.1016/j.cmpb.2020.105673.

[11] S. Singh, R. Repaka, Temperature-controlled radiofrequency ablation of different tissues using two-compartment models, Int. J. Hyperth. 33 (2017) 122–134. https://doi.org/10.1080/02656736.2016.1223890.

[12] S. Singh, A. Bhowmik, R. Repaka, Thermal analysis of induced damage to the healthy cell during RFA of breast tumor, J. Therm. Biol. 58 (2016) 80–90. https://doi.org/10.1016/j.jtherbio.2016.04.002.

[13] S. Yap, E.H. Ooi, J.J. Foo, E.T. Ooi, Bipolar radiofrequency ablation treatment of liver cancer employing monopolar needles : A comprehensive investigation on the efficacy of time-based switching, Comput. Biol. Med. 131 (2021) 104273. https://doi.org/10.1016/j.compbiomed.2021.104273.

[14] S. Yap, E.H. Ooi, J.J. Foo, E.T. Ooi, Comparisons between impedance-based and time-based switching bipolar radiofrequency ablation for the treatment of liver cancer, Comput. Biol. Med. 134 (2021) 104488. https://doi.org/10.1016/j.compbiomed.2021.104488.

[15] M. Dhiman, A.K. Kumawat, Ramjee Repaka, Directional ablation in radiofrequency ablation using a multi-tine electrode functioning in multipolar mode: An in-silico study using a finite set of states, Comput. Biol. Med. 126 (2020) 104007.

https://doi.org/10.1016/j.compbiomed.2020.104007.
[16] M. Edalatifar, M. Bagher, T. Mohammad, F. Setoudeh, Using deep learning to learn physics of conduction heat transfer, J. Therm. Anal. Calorim. 146 (2021) 1435–1452. https://doi.org/10.1007/s10973-020-09875-6.
[17] M. Edalatifar, M. Ghalambaz, M.B. Tavakoli, F. Setoudeh, New loss functions to improve deep learning estimation of heat transfer, Neural Comput. Appl. 34 (2022) 15889–15906. https://doi.org/10.1007/s00521-022-07233-1.
[18] Z. Liu, M. Ahmed, A. Sabir, S. Humphries, S.N. Goldberg, Computer modeling of the effect of perfusion on heating patterns in radiofrequency tumor ablation.pdf, Int. J. Hyper. 23 (2007) 49–58.
[19] M. Ahmed, Z. Liu, S. Humphries, S.N. Goldberg, Computer modeling of the combined effects of perfusion, electrical conductivity, and thermal conductivity on tissue heating patterns in radiofrequency tumor ablation, Int. J. Hyperth. 24 (2008) 577–588. https://doi.org/10.1080/02656730802192661.
[20] D.J. Schutt, D. Haemmerich, Effects of variation in perfusion rates and of perfusion models in computational models of radio frequency tumor ablation, Med. Phys. 35 (2008) 3462–3470. https://doi.org/10.1118/1.2948388.
[21] A. Bhandari, J. Kartikey, S. Anup, W. Zhan, Convection-enhanced delivery of antiangiogenic drugs and liposomal cytotoxic drugs to heterogeneous brain tumor for combination therapy, Cancers (Basel). 14 (2022) 4177. https://doi.org/https://doi.org/10.3390/cancers14174177.
[22] A. Bhandari, A. Bansal, R. Jain, A. Singh, N. Sinha, Effect of tumor volume on drug delivery in heterogeneous vasculature of human brain tumors, ASME J. Eng. Sci. Med. Diagnostics Ther. 2 (2019) 1–10. https://doi.org/10.1115/1.4042195.
[23] A. Singh, M. Haris, D. Rathore, A. Purwar, M. Sarma, G. Bayu, N. Husain, R.K.S. Rathore, R.K. Gupta, Quantification of physiological and hemodynamic indices using T 1 dynamic contrast-enhanced MRI in intracranial mass lesions, J. Magn. Reson. Imaging. 26 (2007) 871–880. https://doi.org/10.1002/jmri.21080.
[24] D. Andreuccetti, N. Zoppetti, Quasi-static electromagnetic dosimetry: from basic principles to examples of applications, Int. J. Occup. Saf. Ergon. 12 (2006) 201–215. https://doi.org/10.1080/10803548.2006.11076682.
[25] S.K. Hall, E.H. Ooi, S.J. Payne, A mathematical framework for minimally invasive tumor ablation therapies, Crit. Rev. Biomed. Eng. 42 (2014) 383 – 417. https://doi.org/10.1615/CritRevBiomedEng.2014011825.
[26] H.H. Pennes, Analysis of Tissue and Arterial Blood Temperatures in the Resting Human Forearm, J. Appl. Physiol. 1 (1948) 93–122. https://doi.org/10.1152/jappl.1948.1.2.93.
[27] F.C. Henriques, A.R. Moritz, Studies of thermal injury: I. The conduction of heat to and through skin and the temperatures attained therein. A theoretical and an experimental investigation., Am. J. Pathol. 23 (1947) 530–549.
[28] J. Pearce, Mathematical models of laser-induced tissue thermal damage, Int. J. Hyperth. 27 (2011) 741–750. https://doi.org/10.3109/02656736.2011.580822.
[29] M.M. De Oliveira, P. Wen, T. Ahfock, Heat transfer due to electroconvulsive therapy : Influence of anisotropic thermal and electrical skull conductivity, Comput. Methods Programs Biomed. 133 (2016) 71–81. https://doi.org/10.1016/j.cmpb.2016.05.022.
[30] T. Abboud, G. Hahn, A. Just, M. Paidhungat, A. Nazarenus, D. Mielke, V. Rohde, An insight into electrical resistivity of white matter and brain tumors, Brain Stimul. 14 (2021) 1307–1316. https://doi.org/10.1016/j.brs.2021.08.023.
[31] D. Haemmerich, L. Chachati, A.S. Wright, D.M. Mahvi, F.T. Lee, J.G. Webster, L. Fellow, Hepatic radiofrequency ablation with internally cooled probes : effect of coolant temperature on

lesion size, IEEE Trans. Biomed. Eng. 50 (2003) 493–500.
[32] J.P. Abraham, E.M. Sparrow, A thermal-ablation bioheat model including liquid-to-vapor phase change, pressure- and necrosis-dependent perfusion, and moisture-dependent properties, Int. J. Heat Mass Transf. 50 (2007) 2537–2544. https://doi.org/https://doi.org/10.1016/j.ijheatmasstransfer.2006.11.045.
[33] S.K. Hall, E.H. Ooi, S.J. Payne, Cell death, perfusion and electrical parameters are critical in models of hepatic radiofrequency ablation, Int. J. Hyperth. 31 (2015) 538–550. https://doi.org/10.3109/02656736.2015.1032370.
[34] M. Trujillo, J. Alba, E. Berjano, Relationship between roll-off occurrence and spatial distribution of dehydrated tissue during RF ablation with cooled electrodes, Int. J. Hyperth. 28 (2012) 62–68. https://doi.org/10.3109/02656736.2011.631076.
[35] E. Ewertowska, R. Quesada, A. Radosevic, A. Andaluz, X. Moll, F.G. Arnas, E. Berjano, F. Burdío, M. Trujillo, R. Quesada, A. Radosevic, A. Andaluz, X. Moll, F. García, A clinically oriented computer model for radiofrequency ablation of hepatic tissue with internally cooled wet electrode, Int. J. Hyperth. 35 (2018) 194–204. https://doi.org/10.1080/02656736.2018.1489071.
[36] A. Singh, R.K.S. Rathore, M. Haris, S.K. Verma, N. Husain, R.K. Gupta, Improved bolus arrival time and arterial input function for tracer kinetic analysis in DCE-MRI, J. Magn. Reson. Imaging. 29 (2009) 166–176. https://doi.org/10.1002/jmri.21624.
[37] A. Gasselhuber, M.R. Dreher, A. Negussie, B.J. Wood, F. Rattay, D. Haemmerich, Mathematical spatio-temporal model of drug delivery from low temperature sensitive liposomes during radiofrequency tumour ablation, Int. J. Hyperth. 26 (2010) 499–513. https://doi.org/10.3109/02656731003623590.
[38] J. Cha, D. Choi, M. Woo, H. Rhim, Y. Kim, L.K. Hyo, Y.H. Jung, P.K. Cheoul, Radiofrequency ablation zones in ex vivo bovine and in vivo porcine livers : Comparison of the use of internally cooled electrodes and internally cooled wet electrodes, Cardiovasc. Interv. Radiol. 32 (2009) 1235–1240. https://doi.org/10.1007/s00270-009-9600-0.
[39] G.H. Bardy, P.L. Sawyer, G.W. Johnson, D.D. Reichenbach, Radio-frequency ablation: effect of voltage and pulse duration on canine myocardium., Am. J. Physiol. 258 (1990) H1899-905. https://doi.org/10.1152/ajpheart.1990.258.6.H1899.
[40] S. Yan, K. Gu, X. Wu, W. Wang, Computer simulation study on the effect of electrode–tissue contact force on thermal lesion size in cardiac radiofrequency ablation, Int. J. Hyperth. 37 (2020) 37–48. https://doi.org/10.1080/02656736.2019.1708482.
[41] K.K. Ng, C.M. Lam, R.T. Poon, T.W. Shek, W.C. Yu, J.Y. To, Y.H. Wo, C.P. Lau, T.C. Tang, D.W. Ho, S.T. Fan, Porcine liver: morphologic characteristics and cell viability at experimental radiofrequency ablation with internally cooled electrodes., Radiology. 235 (2005) 478–486. https://doi.org/10.1148/radiol.2352040425.
[42] A.S.K. Kho, E.H. Ooi, J.J. Foo, E.T. Ooi, The effects of vaporisation, condensation and diffusion of water inside the tissue during saline-infused radiofrequency ablation of the liver: A computational study, Int. J. Heat Mass Transf. 194 (2022) 123062. https://doi.org/10.1016/j.ijheatmasstransfer.2022.123062.
[43] B. Zhang, M.A.J. Moser, E.M. Zhang, Y. Luo, C. Liu, W. Zhang, A review of radiofrequency ablation: Large target tissue necrosis and mathematical modelling, Phys. Medica. 32 (2016) 961–971. https://doi.org/10.1016/j.ejmp.2016.07.092.
[44] S.-M. Lin, C.-J. Lin, H.-J. Chung, C.-W. Hsu, C.-Y. Peng, Power rolloff during interactive radiofrequency ablation can enhance necrosis when treating hepatocellular carcinoma, Am. J. Roentgenol. 180 (2003) 151–157. https://doi.org/10.2214/ajr.180.1.1800151.
[45] J.J. Pérez, J.J. Pérez-Cajaraville, V. Muñoz, E. Berjano, Computer modeling of electrical and thermal performance during bipolar pulsed radiofrequency for pain relief, Med. Phys. 41 (2014)

71708. https://doi.org/https://doi.org/10.1118/1.4883776.

[46] G. Reddy, M.R. Dreher, C. Rossmann, B.J. Wood, D. Haemmerich, Cytotoxicity of hepatocellular carcinoma cells to hyperthermic and ablative temperature exposures: In vitro studies and mathematical modelling, Int. J. Hyperth. 29 (2013) 318–323. https://doi.org/10.3109/02656736.2013.792125.

[47] M. Trujillo, E. Berjano, Review of the mathematical functions used to model the temperature dependence of electrical and thermal conductivities of biological tissue in radiofrequency ablation, Int. J. Hyperth. 29 (2013) 590–597. https://doi.org/10.3109/02656736.2013.807438.

[48] P. Rattanadecho, P. Keangin, Numerical study of heat transfer and blood flow in two-layered porous liver tissue during microwave ablation process using single and double slot antenna, Int. J. Heat Mass Transf. 58 (2013) 457–470. https://doi.org/10.1016/j.ijheatmasstransfer.2012.10.043.

[49] C. Tucci, M. Trujillo, E. Berjano, M. Iasiello, A. Andreozzi, G.P. Vanoli, Pennes' bioheat equation vs. porous media approach in computer modeling of radiofrequency tumor ablation, Sci. Rep. 11 (2021) 1–13. https://doi.org/10.1038/s41598-021-84546-6.

[50] A. Bhandari, A. Bansal, A. Singh, N. Sinha, Perfusion kinetics in human brain tumor with DCE-MRI derived model and CFD analysis, J. Biomech. 59 (2017) 80–89. https://doi.org/10.1016/j.jbiomech.2017.05.017.

[51] A. Bhandari, A. Bansal, A. Singh, N. Sinha, Numerical study of transport of anti-cancer drugs in heterogeneous vasculature of human brain tumors using DCE-MRI, ASME J. Biomech. Eng. 140 (2018) 051010. https://doi.org/10.1115/1.4038746.

[52] A. Bhandari, A. Bansal, A. Singh, R. Kumar, N. Sinha, Comparison of transport of chemotherapeutic drugs in voxelized heterogeneous model of human brain tumor, Microvasc. Res. 124 (2019) 76–90. https://doi.org/10.1016/j.mvr.2019.03.003.

[53] S.M. Yacoob, N.S. Hassan, FDTD analysis of a noninvasive hyperthermia system for brain tumors, Biomed. Eng. Online. 11 (2012) 1–22. https://doi.org/10.1186/1475-925X-11-47.